C. R. Mecanique 345 (2017) 868–889

Contents lists available at ScienceDirect

Comptes Rendus Mecanique

www.sciencedirect.com

Discrete element analysis of the mechanical properties of deep-sea methane hydrate-bearing soils considering interparticle bond thickness

Mingjing Jiang [a,b,c,*], Jie He [a,b,c], Jianfeng Wang [d], Yaping Zhou [a,b,c], Fangyuan Zhu [a,b,c]

[a] State Key Laboratory of Disaster Reduction in Civil Engineering, Tongji University, Shanghai 200092, China
[b] Department of Geotechnical Engineering, Tongji University, Shanghai 200092, China
[c] Key Laboratory of Geotechnical and Underground Engineering of Ministry of Education, Tongji University, Shanghai 200092, China
[d] Department of Civil and Architectural Engineering, City University of Hong Kong, Hong Kong

ARTICLE INFO

Article history:
Received 13 February 2016
Accepted 13 September 2017
Available online 4 October 2017

Keywords:
Discrete element method
Methane hydrate-bearing soil
THM bond model
Inter-particle bond thickness
Mechanical behavior

ABSTRACT

Due to increasing global energy demands, research is being conducted on the mechanical properties of methane hydrate-bearing soils (MHBSs), from which methane hydrate (MH) will be explored. This paper presents a numerical approach to study the mechanical properties of MHBSs. The relationship between the level of MH saturation and the interparticle bond thickness is first obtained by analyzing the scanning electron microscope images of MHBS samples, in which is the bridge connecting the micromechanical behavior captured by the DEM with the macroscopic properties of MHBSs. A simplified thermal-hydromechanical (THM) bond model that considers the different bond thicknesses is then proposed to describe the contact behavior between the soil particles and those incorporated into the discrete element method (DEM). Finally, a series of biaxial compression tests are carried out with different MH saturations under different effective confining pressures to analyze the mechanical properties of deep-sea MHBSs. The results of the DEM numerical simulation are also compared with the findings from triaxial compression tests. The results show that the macromechanical properties of deep-sea MHBSs can be qualitatively captured by the proposed DEM. The shear strength, cohesion, and volumetric contraction of deep-sea MHBSs increase with increasing MH saturation, although its influence on the internal friction angle is obscure. The shear strength and volumetric contraction increase with increasing effective confining pressure. The peak shear strength and the dilation of MHBSs increase as the critical bond thickness increases, while the residual deviator stress largely remains the same at a larger axial strain. With increasing the axial strain, the percentage of broken bonds increases, along with the expansion of the shear band.

© 2017 Académie des sciences. Published by Elsevier Masson SAS. All rights reserved.

* Corresponding author.
E-mail address: mingjing.jiang@tongji.edu.cn (M. Jiang).

https://doi.org/10.1016/j.crme.2017.09.003
1631-0721/© 2017 Académie des sciences. Published by Elsevier Masson SAS. All rights reserved.

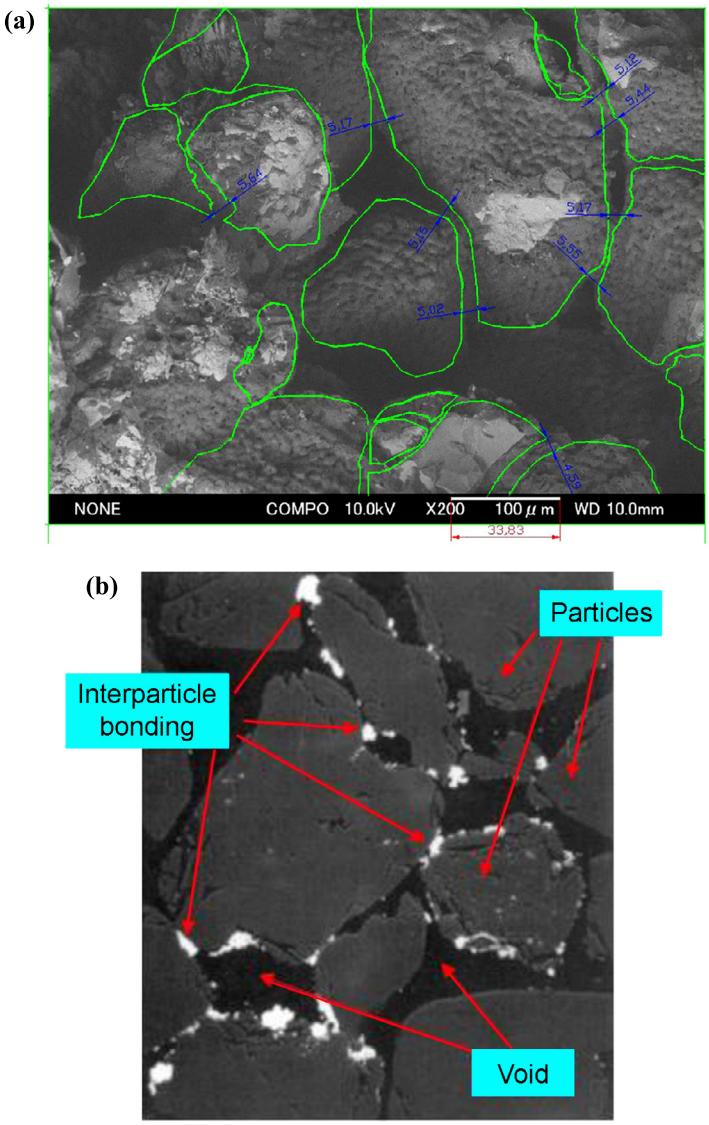

Fig. 1. SEM images: (a) MH bonds in the methane hydrate-bearing soil [11]; (b) inter-particle bonds in the natural sands [12].

1. Introduction

Methane hydrate-bearing soils (MHBSs), which are natural soil deposits that contain methane hydrate (MH) inside their pores, are abundantly available in the continental margins and permafrost regions [1]. MH is recognized as one of the most promising resources for resolving the current energy crisis [2]. Due to the increasing global energy demand, significant research attention is being directed toward examining the physical, chemical and mechanical properties of MHBSs, and devising methods to quantify and identify MH-bearing deposits [3]. However, commercial exploitation of these deposits could have catastrophic effects, such as submarine landslide and Tsunami. Therefore, the study of the mechanical properties of MHBSs is of great significance from a geotechnical point of view [4].

Previous studies show that the mechanical characteristics of MH-bearing sediments are highly dependent on the hydrate morphology [5,6]. According to the MH morphology, MHBSs are generally categorized as either pore filling or cementing, depending on where the MH is formed in the pore space [7]. MH-bearing sediments are easily formed by cementing in gas-rich environments and, in general, the MH in the cementing type has a greater effect on the ensemble strength and stiffness of the MHBSs, especially at lower MH saturation values, compared with the pore-filling type [5–7]. Very little research has examined the cementing type soil [8–10]. This constitutes one of the strong motivations of this paper.

Fig. 1a presents a scanning electron micrograph (SEM) of a MH-bearing sample, in which different bond thicknesses of MH can be observed among the soil particles [11]. Fig. 1b provides a SEM of a Lower Green natural sand sample obtained by

Cuccovillo and Coop [12], in which the cement colored in white forms interparticle bonds that weld the particles together. Therefore, as illustrated in Fig. 1, MH-bearing sediments and natural soils share a similar microstructure. It is universally acknowledged by geo-researchers that the mechanical behaviors of such cemented geomaterials are controlled not only by the stress history and density, as described by classical geo-mechanics, but also influenced by the strength of the bonds between the soil particles [13–23]. Though numerous continuum constitutive models have been proposed by different scholars [24–32] to elaborate some crucial features of natural soils, no particular model or theory has received universal acceptance, mostly due to the lack of quantitative information on the effects of cementing. This situation clearly extends to studies of MHBSs.

In geo-laboratory research, two types of samples are used to investigate the mechanical behavior of MH-bearing soils: natural MHBS samples retrieved from the field, e.g., [33–41], and synthetic MH-bearing samples, e.g., [42,43,11,44–51]. Although special sampling devices have been developed to maintain the water pressure and temperature encountered in situ [52,53], it is difficult to obtain natural MH soil cores in an intact state, as the MH can easily dissociate during coring and sampling, either through a reduction in water pressure or an increase in temperature [3]. In addition, to obtain reliable results, laboratory experiments with synthetic MHBS samples require strict low-temperature and high-pressure conditions that can reflect the real MHBS environment, which is also a challenge for the testing equipment. Moreover, even with advanced technologies, such as X-rays [54], the stereophotogrammetric technique [55], or particle image velocimetry [56], quantitative data on all the bonds are still unobtainable within the samples. Hence, although significantly important, it is not yet clear to quantitatively describe the bonding effects and to understand their links with the microstructure of MHBS obtained experimentally.

The discrete element method (DEM), originally developed for dry granular materials by Cundall and Strack [57], treats soils as an assembly of discrete materials, and starts with the contact laws of interparticle contacts to provide macroscopic/microscopic responses of the soil assembly under different loading conditions. The interactions between particles are controlled by contact law. The motion of each particle is determined by Newton's second law. In addition to facilitating sample reproducibility and being able to monitor the evolution of internal stresses in a nondestructive manner, the DEM appears to be a promising tool to understand the relation between the bond properties at particle contacts and the observed macroscopic behavior. DEM has been employed to examine several aspects of soil behavior, such as creep theory [58], anisotropy [59] of soils, and constitutive models for granular material [19]. It has also been employed to investigate boundary value problems such as the penetration mechanism of cone-penetration tests [60], slope instability [61] and retaining wall [62]. Furthermore, DEM can be coupled with other numerical methods such as Computational Fluid Dynamics [63]. It is believed that, by providing a better understanding of the mechanical behavior of MHBSs, the DEM can help establish an appropriate constitutive model.

Jiang et al. [8] proposed a simple bond model based on the experimental data from microscopic mechanical tests and implemented it into a two-dimensional DEM code, NS2D. The DEM incorporating the model captured the main characteristics of MHBSs in a series of drained biaxial compression tests. However, the model only includes the normal and tangential behavior, and ignores the mechanical response of the bond-rolling resistance of soil particles. In addition, the model did not clarify the exact correlation between MH saturation and bond strength for simplicity. To reflect the effect of the real environment on the properties of MHBSs, [9,10] further proposed a bond contact model that considers the MH density, temperature and water pressure, which is implemented into the DEM to examine the effects of MH saturation, the effective confining pressure and back pressure (initial pore water pressure) on the macromechanical properties of MHBSs. The contact model proposed captures the effects of bonding on the mechanical properties of MHBSs and is helpful for understanding the relationship between the micro-mechanisms and macromechanical behavior of MHBSs. Nevertheless, the contact model treats the bond thickness of MH between particles as a constant value (i.e. the thickness at the center, t_0), and does not consider the variation in the bond thickness between particles illustrated in Fig. 1a. Accordingly, reducing the difference between the model assumptions and the actual situation constitutes another strong motivation for our study.

MH forms between soil particles as a cementing material, and the bond size is directly connected to the level of MH saturation, which further affects the mechanical behavior of MHBSs. In this study, the relationship between the MH saturation and the interparticle bond thickness is first obtained by analyzing the SEMs of MHBS samples observed by other scholars [11,64], connecting the micro-macro properties of MHBSs.

Next, a simplified thermal-hydromechanical (THM) bond model, which considers the variation in the bond thickness between soil particles, is established based on the mechanical responses of the contact model [22,65,9] in relation to environmental parameters, namely temperature T, water pressure σ_w, and MH density ρ.

Finally, a series of drained biaxial compression tests are simulated to investigate the mechanical properties of deep-sea MHBSs by the DEM, where the simplified THM bond thickness model compiled by the C++ code is implemented. In addition, the results from the DEM numerical simulation are compared with the triaxial experimental observations of Masui et al. [46].

2. Relationship between bond thickness and MH saturation

MH saturation is defined by the ratio of MH to the total pore volume, namely:

$$S_{MH} = \frac{V_{MH}}{V_V} \times 100\% \tag{1}$$

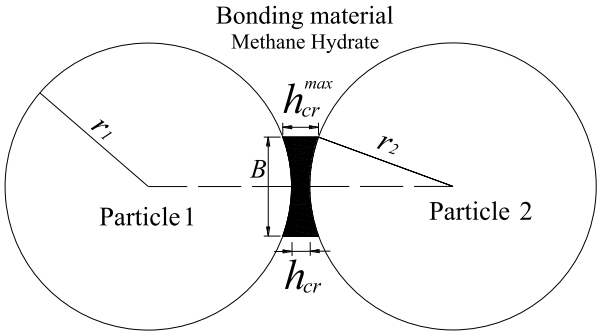

Fig. 2. Simplified MH-bonding granules in the cementing type of MHBS.

where V_{MH} is the volume of MH and V_V is the total pore volume (including the MH).

It is difficult to analyze the microscale features of MHBSs using conventional experimental methods due to their metallogenic geological conditions. However, many useful explorations have been conducted in this area [11,64,66].

Jin et al. [64,66] used a microfocus X-ray CT apparatus with a higher spatial resolution to image the 2D and 3D fabric of MHBSs to study their scale characteristics. The 2D and 3D images obtained clearly show the spatial distribution of the sand particles, MH, and empty pores. Hyodo et al. [11] studied the microstructure of different MH saturation samples using low-temperature SEM technology. The SEM images of the different MH saturations show that some gaps exist in the bonded MH at particle contact. In other words, the bond thickness varies between soil particles, and the gap does not exceed a certain value (i.e. the critical bond thickness, h_{cr}^{max}) when MH forms in the cementing type of MHBS samples. Fig. 2 presents simplified MH-bonding granules in the cementing type of MH-bearing soil. As shown in Fig. 2, the contact soil particles are simplified as discs, particle 1 and particle 2 with radii r_1 and r_2, respectively, in which the h_{cr}^{max} is the maximum bond thickness of the contact between two particles. When the gap between soil particles is smaller than the value of h_{cr}^{max}, MH can form to bond the soil particles. The parameter h_{cr} is the minimum bond thickness connecting the center points of two particles. B represents the bond width, varying along the disk surface, and is determined based on the geometric analysis.

$$B = \sqrt{4r^2 - \left(2r - h_{cr}^{max} + h_{cr}\right)^2} \tag{2}$$

where r is the common radius, and can be calculated by the equation $r = 2r_1r_2/(r_1 + r_2)$.

The relationship between S_{MH} and h_{cr}^{max} can be established based on statistical analyses of the existing SEMs of MHBS samples (i.e. the microscopic images of 30%, 50% MH saturation obtained by Hyodo et al. [11] and 86.3% MH saturation from Jin et al. [64]).

Hyodo et al. [11] used a fine sand sample in which the particle size distribution is in the range of 0.09–0.4 mm with an average particle diameter d_{50} of 0.2 mm, while Jin et al. [64] used a sand classified as a medium and fine grain, with a particle size distribution in the range of 0.01–1 mm ($d_{50} = 0.32$ mm). Although the particle size distributions are different, both samples represent fine-to-medium-sized sand free from clay soil. Therefore, MH formation is independent of the influence of the difference in particle size. In addition, the porosity of the two samples is both 40%. Because of the different average particle sizes, it is rational to normalize h_{cr}^{max} by dividing it over d_{50}.

Fig. 3 provides microscopic images of a MHBS sample obtained by Hyodo et al. [11], in which Fig. 3(a) is a pure sand sample that does not include MH and Fig. 3(b) is the SEM of the same sample with 50% MH saturation. The concept of 'contour translation coverage', which stems from the simplified quantitative analysis method of Shi [67] for analyzing the microstructures of clayed soils, is adopted to determine the micro-bond sizes of MH. The contour of the clearly distinguishable particles and pores without MH translates to the same points on the microscopic image, with 50% MH saturation to measure the corresponding MH bond size. First, CAD software is used to depict the outline of the main particles in a sample without MH. The outline contour is then translated to the same location over the sand sample of 50% MH saturation. Finally, the MH bond thicknesses formed between the particles are measured and converted into the actual size according to a scaling relation. Table 1 presents the MH bond thicknesses between the particles marked in Fig. 3(b). The size h_{cr}^{max} was obtained from the length scale provided along the image. As illustrated in Fig. 3(b), there exists a red number (i.e. 33.83) at the bottom, and the value of 33.83 represents a real length of 100 μm. Then the natural size can be calculated from the image size multiplying it by this factor (i.e. 100/33.83). The mean value of the eight groups of natural sizes is 15.6 μm. To reduce the manual measurement error, the average value of 15.6 μm is used as the value of h_{cr}^{max} for the 50% MH saturation sample.

Fig. 4 shows a SEM image of a 30% MH saturation sample obtained by Hyodo et al. [11]. As illustrated in Fig. 4, the blue number is 16.9 at the bottom, and the value of 16.9 represents a real length of 100 μm. Then the natural size can be calculated by the image size by multiplying it by this factor (i.e. 100/16.9). The mean value of the twelve groups of natural sizes, illustrated in Table 2, is 8.13 μm.

Fig. 5(a) presents an X-ray CT image obtained by Jin etal. [64] in which sand particles, MH regions, and empty pores are colored in light gray, green, and blue in the electronic edition, respectively. The procedure for processing the image

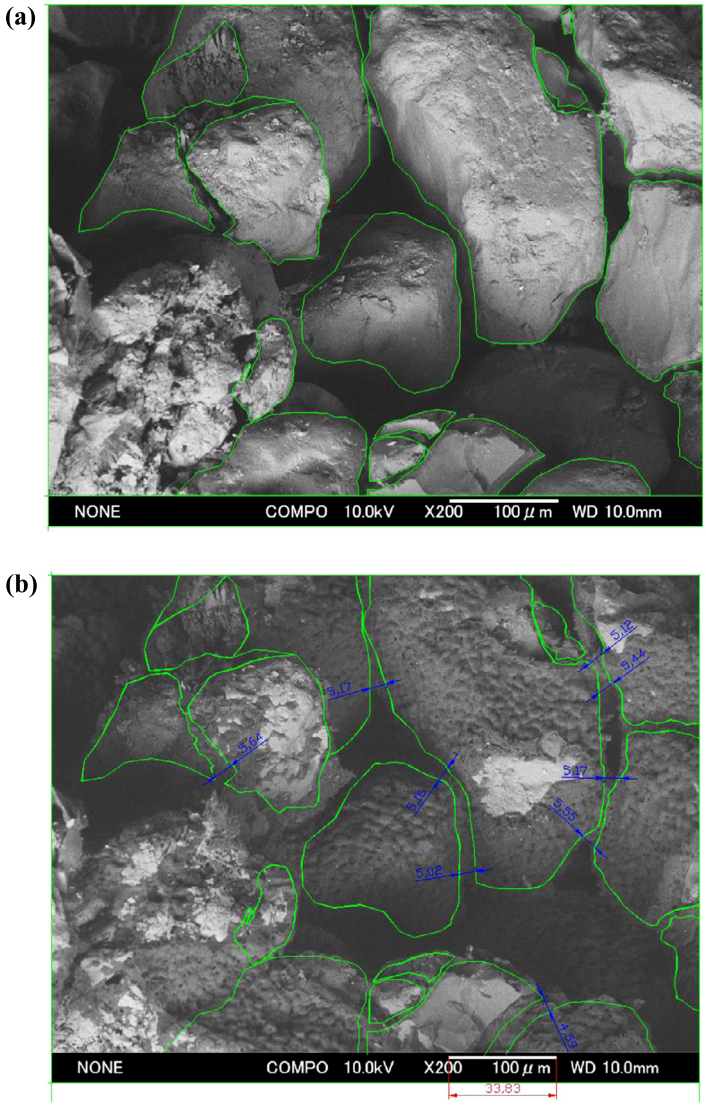

Fig. 3. SEM image of an MHBS obtained by Hyodo et al. [11]: (a) the sand specimen without MH; (b) 50% MH saturation of the MHBS specimen.

Table 1
Bond thickness values of S_{MH} = 50% MH saturation (the unit of natural size: μm).

Image size	5.64	5.17	5.16	5.02	5.55	5.17	5.44	5.12
Natural size	16.7	15.3	15.3	14.8	16.4	15.3	16.1	15.1

Table 2
Bond thickness values of S_{MH} = 30% MH saturation (the unit of natural size: μm).

Image size	1.33	1.43	1.4	1.39	1.28	1.34
Natural size	16.7	15.3	15.3	14.8	16.4	15.3
Image size	1.44	1.32	1.31	1.31	1.4	1.54
Natural size	16.1	15.1	7.75	7.75	8.28	9.11

is as follows. First, CAD software is used to draw the contours of the sand particles and the empty pores using blue and green-colored lines respectively, as illustrated in Fig. 5(b). The total area of the particles S_s and of the pores S_o, as well as the total area of the representative sample S are then measured, and the MH saturation can be calculated using the equation $S_{MH} = (S - S_s - S_o)/(S - S_s)$. In this case, the average hydrate bond thickness is about 30.7 μm, which corresponds to the value of h_{cr}^{max} for the 86.3% MH saturation sample.

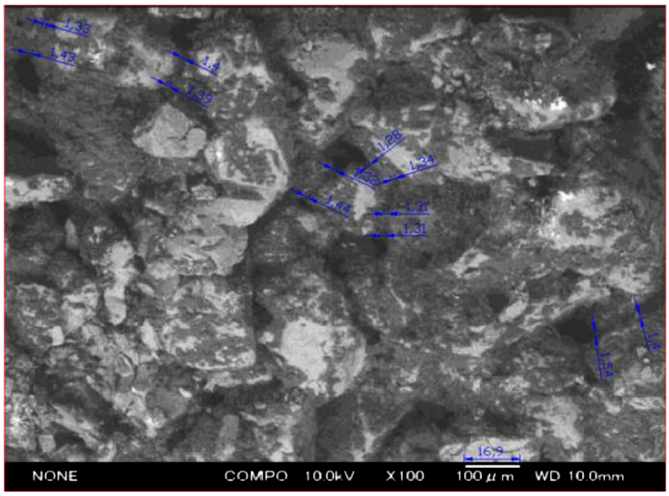

Fig. 4. SEM of 30% MH saturation of an MHBS specimen [11].

In these three MH saturation samples (i.e. 30%, 50%, and 86.3%), the porosity of the samples is 40%, and the d_{50} of the 30%, 50% MH saturation samples is both 0.2 mm, while the d_{50} of the 86.3% MH saturation sample is 0.32 mm. To eliminate the influence of the d_{50}, $h_{\mathrm{cr}}^{\max}$ is normalized by dividing it over d_{50}. Fig. 6 provides the relationship between the normalized critical bond thickness $h_{\mathrm{cr}}^{\max}$ and the MH saturation S_{MH}, which shows that the $h_{\mathrm{cr}}^{\max}$ gradually increases nonlinearly up to a constant value with increasing MH saturation.

One can note in Fig. 6 that the value of $h_{\mathrm{cr}}^{\max}$ equals zero when MH saturation falls below 20%. Previous studies [6,5,68] have shown that MH preferentially forms at the particle surface in gas-rich MH-bearing sediments. The bonding effect of the MH attached to the particle surface is not as strong as that of the MH cemented between particles. This is also validated by the relationship between the deviator stress and axial strain of the MH-bearing samples obtained by Hyodo et al. [11]. The deviator stress of the 24.2% MH saturation sample is always slightly higher than that without MH, while the deviator stress of the 35.1% and 53.1% MH saturation samples increases clearly with MH saturation. In addition, when the hydrates nucleate on the boundaries of sediment particles and grow freely into pore spaces, the effect of MH saturation on the strength characteristics of MHBSs is of little significance. When MH saturation is less than 20%, the bonding effects are not obvious. So, we assume that when the MH saturation is less than 20%, the value of $h_{\mathrm{cr}}^{\max}$ between the particles is zero.

The parameter $h_{\mathrm{cr}}^{\max}$ is the maximum bond thickness of the contact between two particles; d_{50} is the mean diameter of the soil. Since the particle size distributions used by Jin et al. [64] and Hyodo et al. [11] are different, the obtained value of $h_{\mathrm{cr}}^{\max}$ will be different and restrictedly useful. Hence, $h_{\mathrm{cr}}^{\max}$ is normalized by dividing d_{50}, which may provide valuable guidance for future researches. Certainly, a different size parameter (e.g., d_{10}, d_{60}) can be chosen too for normalization. The fitting relation between $h_{\mathrm{cr}}^{\max}/d_{50}$ and S_{MH} can be expressed by Equation (3), which meets the continuity requirement.

$$\frac{h_{\mathrm{cr}}^{\max}}{d_{50}} = \begin{cases} 0 & S_{\mathrm{MH}} \le 20\% \\ -0.3268S_{\mathrm{MH}}^2 + 0.4879S_{\mathrm{MH}} - 0.0815 & 20\% < S_{\mathrm{MH}} \le 70\% \\ 0.1 & S_{\mathrm{MH}} > 70\% \end{cases} \tag{3}$$

Based on Hyodo's SEM photos at the particle scale, MH bonds exist at the gap of neighboring particles. With the increase of MH saturation, bond thickness would increase as the bond size B increases. Besides, more particle pairs would be newly bonded by MH as the increased MH fills greater gap. $h_{cr}^{\max}$ dependency on the MH saturation degree is a depiction of this physical process. The $h_{\mathrm{cr}}^{\max}$ dependency on the MH saturation degree, as shown in Eq. (3), is obtained by analyzing the SEM images of the MHBS (Figs. 3–5). It is admitted that the relation drawn in Fig. 6 is greatly limited by the number of SEM images of the MHBS. However, the fact that $h_{\mathrm{cr}}^{\max}/d_{50}$ gradually increases nonlinearly up to a constant value with increasing MH saturation is used in this study as a possible link between particle scale and sample scale.

It should be noted the relationship between $h_{\mathrm{cr}}^{\max}/d_{50}$ and S_{MH}, established based on real (3D) particle-scale images, was used as a possible law linking the macroscopic methane hydrate content and the microscopic contact geometry. In 2D DEM simulations, this cross-scale law borrowed from 3D samples at least provides the right way how $h_{\mathrm{cr}}^{\max}$ varies with S_{MH}, that is, $h_{\mathrm{cr}}^{\max}$ increases with S_{MH} at a decreasing rate, not a constant or increasing one. Even though the law may not be accurate, it is quite useful to study the mechanism of MHBS behavior with affordable samples of large enough amounts of particles in 2D. Actually, due to the fictitious nature of 2D DEM simulation itself, there is no such cross-scale law to be claimed 'accurate' for 2D simulations. With the above consideration, the 3D-based cross-scale law was qualitatively applied in this 2D simulation.

Note that because the occurrence of MHBSs requires strict high-pressure and low-temperature conditions, it is an extremely expensive and also technical challenge to take undisturbed samples from the deep seabed. Moreover, the detail of

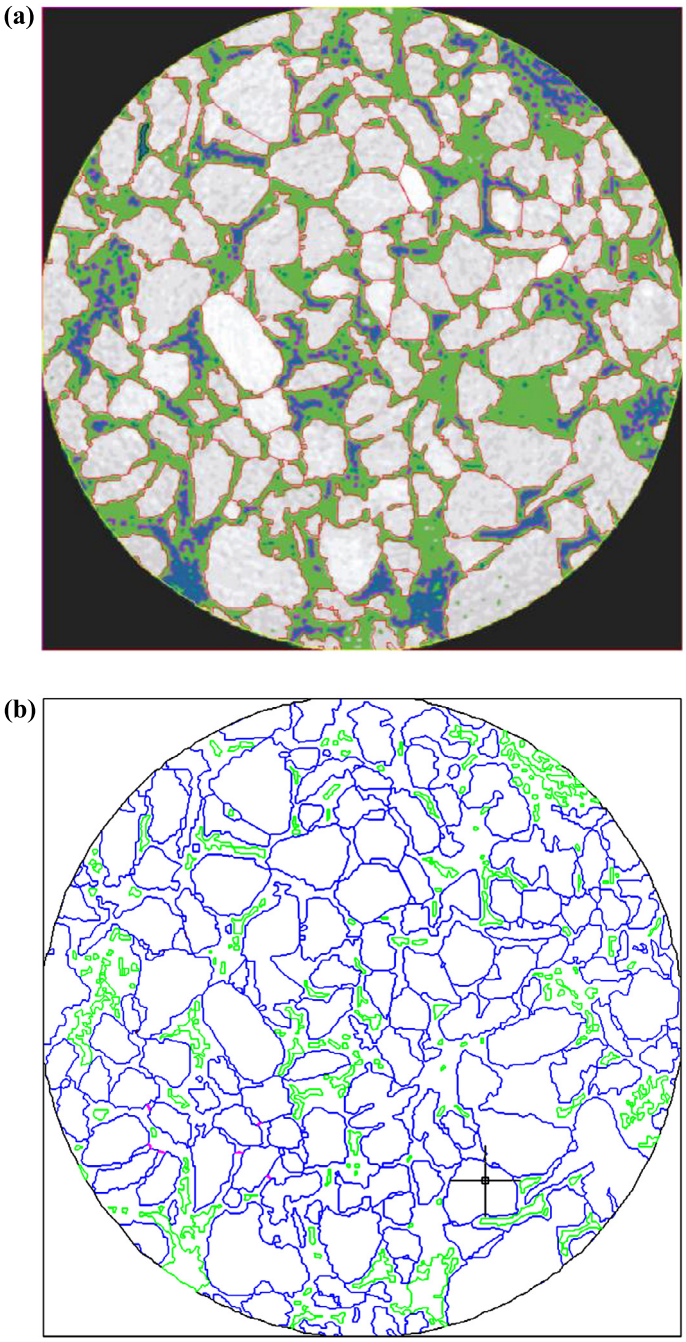

Fig. 5. MHBS specimen used by Jin et al. [64]: (a) SEM image; (b) outline of the sample.

the SEM images of MHBS samples is greatly limited, thereby constraining the amount of micro-size information. Therefore, Equation (3), proposed based on the currently available experimental data, may need further improvement in the future. However, Equation (3) is the bridge connecting the micromechanical behavior captured by the DEM to the macroscopic properties of MHBSs.

It is thus assumed that the bond between the particles affects the mechanical properties of the cementing-type MHBSs only when the MH saturation exceeds 20%. Therefore, the volume of MH V_{bMH} between particles can be calculated by the following equation:

$$V_{\mathrm{bMH}} = V_{\mathrm{V}} \times (S_{\mathrm{MH}} - 20\%) = \frac{eV}{1+e} \times (S_{\mathrm{MH}} - 20\%) \tag{4}$$

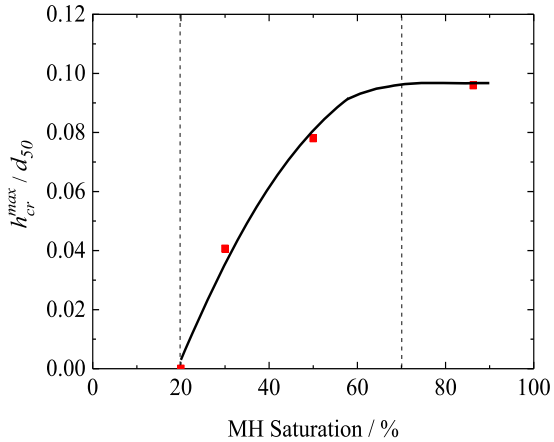

Fig. 6. Relationship between the normalized hydrate critical bond thickness $h_{\mathrm{cr}}^{\max}/d_{50}$ and MH saturation S_{MH}.

In the two-dimensional DEM simulation, MH saturation is defined as the ratio of the area of MH to the total pore area. Accordingly, the bond area of a single contact can be calculated by Equation (5):

$$S_i = \frac{1}{2}\left(h_{\mathrm{cr}}^{\max} + h_{\mathrm{cr}}\right)B + Br - 2r^2 \arctan \frac{B}{\sqrt{4r^2 - B^2}} \tag{5}$$

Hence, the total bond area S_{bMH} of MH-bearing sediments is calculated using Equation (6):

$$S_{\mathrm{bMH}} = \sum_{i=1}^{N} S_i = \sum_{i=1}^{N}\left(\frac{1}{2}\left(h_{\mathrm{cr}}^{\max} + h_{\mathrm{cr}}\right)B + Br - 2r^2 \arctan \frac{B}{\sqrt{4r^2 - B^2}}\right) \tag{6}$$

where N is the total number of contact bonds in the two-dimensional DEM MHBS sample.

3. A bond contact model considering the MH bond thickness

Fig. 7 presents the mechanical response of a bond contact model [9] in three directions. The rationality of the model has been validated by experimental data [22,65]. The normal force F_{n}, the shear force F_{s}, and the moment M for an intact bond are calculated by Equation (7a), (7b), (7c), respectively.

$$F_{\mathrm{n}} = k_{\mathrm{bn}}(u_{\mathrm{n}} - u_0) \tag{7a}$$

$$F_{\mathrm{s}} \leftarrow k_{\mathrm{bs}}\Delta u_{\mathrm{s}} + F_{\mathrm{s}} \tag{7b}$$

$$M \leftarrow k_{\mathrm{bm}}\Delta\theta + M \tag{7c}$$

where u_{n} is the inter-particle overlap; u_0 is the value of u_{n} at the moment of bond formation (i.e. bond equilibrium); Δu_{s}, and $\Delta\theta$ are the increments of the relative shear displacement and relative rotation angle, respectively. k_{bn}, k_{bs}, and k_{bm} are the normal, tangential, and rolling bond stiffness, respectively. The method to calculate these stiffness parameters for bonds will be elaborated in the latter part.

When the force/moment exceeds the bond strength in any direction, the bond breaks in a fragile manner. In this case, the contact laws between the un-bonded grains are as follows:

$$F_{\mathrm{n}} = k_{\mathrm{n}}u_{\mathrm{n}} \tag{8a}$$

$$F_{\mathrm{s}} \leftarrow \min[k_{\mathrm{s}}\Delta u_{\mathrm{s}} + F_{\mathrm{s}}, \mu F_{\mathrm{n}}] \tag{8b}$$

$$M \leftarrow \min\left[k_{\mathrm{m}}\Delta\theta + M, \frac{1}{6}F_{\mathrm{n}}B\right] \tag{8c}$$

where min[·] is the operator taking the minimum value; k_{n}, k_{s}, and k_{m} are the normal, tangential, and rolling contact stiffness of the uncemented soil particles, respectively; μ is the interparticle friction coefficient.

Note that Eq. (8c) is deduced theoretically in our previous study [18], in which the couple M at the contact is $M = \frac{2F_n^3}{3B(K_n\theta)^2}$, where F_{n} and B have the same meaning with that of this paper, K_{n} is the normal stiffness. $\theta = \frac{2F_{\mathrm{n}}}{K_{\mathrm{n}}l}$, l is the contact width, which is still distributed with the remaining intact point-bonds when two particles relatively rotate. When the first breakage happens, $l = B$, and $M = \frac{1}{6}F_{\mathrm{n}}B$. Therefore, the prefactor 1/6 is obtained based on mathematical derivation. The physical scenario of the rolling resistance concept is as follows. Two discs are considered interacting through a finite

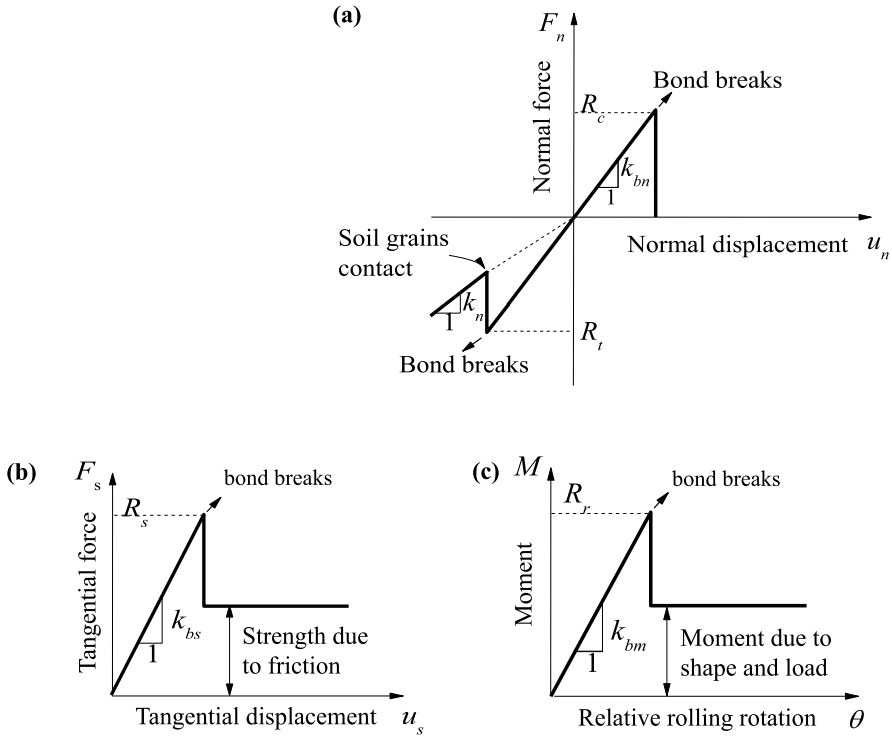

Fig. 7. The mechanical response of a bond contact model: (a) normal direction; (b) tangential direction; (c) rolling direction.

length B, instead of a point, so that the moment can be transferred between the two particles. In this way, the mechanical effects of particle shape angularity on soil behavior can be efficiently simulated with DEM. See a detailed mathematic derivation and the related simplification in Jiang et al. [18].

In addition to breaking purely in the normal, tangential or rolling direction, the MH bond can break through combined interactions in all three directions, which is the general case for most contacts. When the MH bond is simultaneously subject to F_n, F_s, and M, the strength criterion can be represented as a three-dimensional strength envelope in the F_n–F_s–M space, as illustrated in Fig. 8(a). Fig. 8(b) and Fig. 8(c) show the bond strength envelopes, in which the tangential bond strength R_s and rolling bond strength R_r can be expressed as:

$$R_s = f_s \times K_s \times (F_n + R_t) \times \left(\ln\left(\frac{R_c + R_t}{F_n + R_t}\right)\right)^{0.59} \tag{9a}$$

$$R_r = f_r \times K_r \times (F_n + R_t) \times \left(\ln\left(\frac{R_c + R_t}{F_n + R_t}\right)\right)^{0.59} \tag{9b}$$

where R_c and R_t represent the compression and tension bond strengths, respectively. Parameters f_s, K_s, f_r, and K_r are the fitting functional relationships with bond thickness h_{cr} connecting the center points of two particles in the experiment using aluminum rods glued by a cementing agent, which can be calculated by Equation (10a)–(10d).

$$f_s = 2.05\text{–}0.89 \times e^{-(1000h_{cr}-1.15)^2} \tag{10a}$$

$$K_s = 0.41\text{–}61.07h_{cr} \tag{10b}$$

$$f_r = 2.05\text{–}0.92 \times e^{-(1000h_{cr}-1.15)^2} \tag{10c}$$

$$K_r = 0.83\text{–}146.36h_{cr} \tag{10d}$$

When the bond between the soil particles is broken, one grain comes into contact with a new particle. The residual tangential bond strength R_{sr} and the residual rolling bond strength R_{rr} can be obtained using Equation (8a).

The compression and tension bond strengths R_c and R_t are calculated by Equation (11) below according to the experimental results of idealized bonded granules with three different bond thickness values (i.e. 0.6 mm, 1.0 mm, and 1.5 mm) [65].

$$R_t = R_{t0} + 2.67 \times 10^5 h_{cr} \tag{11a}$$

$$R_c = R_{c0} - 4.18 \times 10^6 h_{cr} \tag{11b}$$

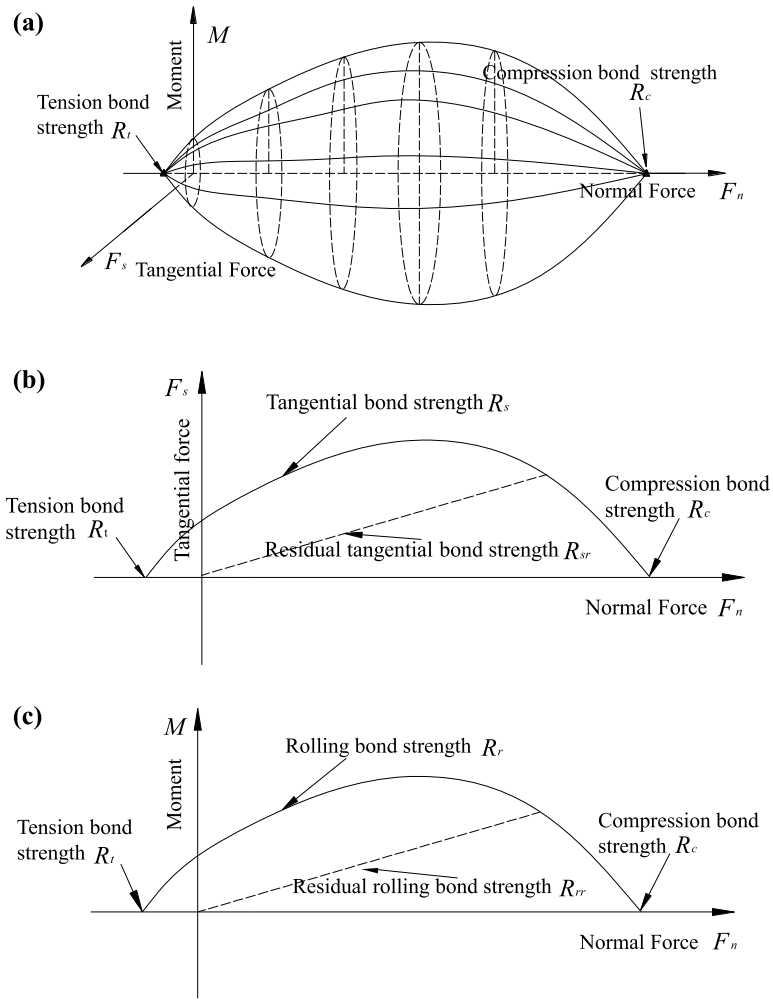

Fig. 8. Bond strength envelope derived from laboratory data: (a) three-dimensional space envelope for the normal/tangential/moment strength F_n–F_s–M; (b) the tangential bond strength envelope for R_s; (c) the rolling bond strength envelope for R_r.

where R_{t0} and R_{c0} are the MH bond tensile and compressive strength when h_{cr} is equal to 0.0 mm. Note that the values of R_{t0} and R_{c0} are not equal to zero.

Eq. (3) was proposed from a MHBS sample test, which is exactly the material simulated in this work. Eqs. (9)–(11) was proposed based on interparticle bond test results with cement as the bond material. Because the MH bond strength between two particles has not been systematically tested so far, two types of bond materials (cement and epoxy resin) were tested in our previous study, and it was found that cement can be used to represent MH. In the laboratory, aluminum rods are bonded with cement. Similarly, in our simulation, sand particles are bonded with methane hydrate. Therefore, Eqs. (9)–(11) obtained from experimental data can be applied to DEM simulation. Detailed information on the following equation can be read from Jiang et al. [65,69].

In the micro-bonded granules experiments, calcium aluminate cement (CA-50), mainly consisting of hydraulic calcium aluminates, is used as the cementing agent between the aluminum rods because of its quick hardening property. This type of cement (CA-50) is nearly equivalent to the type-M cement based on ASTM C845-04 [70]. According to the GB 201-2000 standard [71], the compressive strength of the calcium aluminate cement mortar obtained by the standard measurement method using the standard prismatic sample (i.e. width × length × height: 40 mm × 40 mm × 80 mm) is 50 MPa. The bond compression strength obtained in the bonded aluminum rods tests is about 150 MPa for a bond thickness of 0.6 mm and the strength is approximately treble that of CA-50 (i.e. 50 MPa). This is possibly a result of the size and shape effect (prismatic sample versus inter-particle bond). Therefore, it is assumed that the compressive and tensile strengths of the micro-bond are calculated by multiplying the strength of the macroscopic triaxial samples by three. The micro-bond strength of MH can be calculated in the same way. The feasibility of this approach has been verified in previous studies [9,72]. The micro-bond compressive and tensile strength of the 0.6-mm bonds are calculated as follows:

$$R'_{\mathrm{t}} = 3A \times q_{\mathrm{max,t}} = 3 \times 1 \times B \times q_{\mathrm{max,t}} \tag{12a}$$

$$R'_{\mathrm{c}} = 3A \times q_{\mathrm{max,c}} = 3 \times 1 \times B \times q_{\mathrm{max,c}} \tag{12b}$$

where A is the stress surface area; and B is the surface width of the stress, i.e. the MH bond width.

Under the conditions described in the literature [46], which comprise a temperature of 5 °C, a pore pressure of 8 MPa, and a hydrate density of 0.9 g/cm^3, the tensile and compressive strengths of a MH sample are 4.74 MPa and 8.57 MPa, respectively, based on the following Equation (13) for calculating the maximum deviator of MH, which is strongly related to temperature T, water pressure σ_w, and MH density ρ. The details of the formula derivation can be found in Jiang et al. [9].

$$q_{\mathrm{max,c}}/p_{\mathrm{a}} = 0.81(\sigma_{\mathrm{w}}/p_{\mathrm{a}}) - 2.08(T/T_0) + 184.16(\rho/\rho_{\mathrm{w}}) - 134.65 \tag{13a}$$

$$q_{\mathrm{max,t}}/p_{\mathrm{a}} = 0.45(\sigma_{\mathrm{w}}/p_{\mathrm{a}}) - 1.15(T/T_0) + 101.75(\rho/\rho_{\mathrm{w}}) - 74.39 \tag{13b}$$

where p_{a} is the standard atmospheric pressure (1.01×10^5 Pa), T_0 equals 1 °C , and ρ_{w} is the density of water at 4 °C .

Combining Equation (11) and Equation (12), the values of R_{t0} and R_{c0} can be calculated as follows:

$$R_{\mathrm{t0}} = 1.421 \times 10^7 \times B - 160.2 \tag{14a}$$

$$R_{\mathrm{c0}} = 2.571 \times 10^7 \times B + 2508 \tag{14b}$$

Therefore, the MH tension and compression bond strength considering the bond thicknesses are obtained by combining Equation (11) and Equation (14) as follows. Then, the values of R_{s} and R_{r} can be computed based on Equation (9).

$$R_{\mathrm{t}} = 1.421 \times 10^7 \times B + 2.67 \times 10^5 \times h_{\mathrm{cr}} - 160.2 \tag{15a}$$

$$R_{\mathrm{c}} = 2.571 \times 10^7 \times B - 4.18 \times 10^6 \times h_{\mathrm{cr}} + 2508 \tag{15b}$$

Under the normal force F_{n}, the overall deformation δ is composed of two parts: the particle deformation δ_1 and the hydrate deformation δ_2. To simplify the calculation, it is assumed that the stiffness of the two particles is both equal to k_{n} and that MH stiffness equals k_{mh}. The normal bond stiffness k_{bn} can then be calculated by Equation (16), based on the deformation of the particles and of the MH:

$$k_{\mathrm{bn}} = \frac{F_{\mathrm{n}}}{\delta} = \frac{F_{\mathrm{n}}}{\delta_1 + \delta_1} = \frac{F_{\mathrm{n}}}{2F_{\mathrm{n}}/k_{\mathrm{n}} + F_{\mathrm{n}}/k_{\mathrm{mh}}} = \frac{k_{\mathrm{n}}k_{\mathrm{mh}}}{k_{\mathrm{n}} + 2k_{\mathrm{mh}}} \tag{16}$$

where the stiffness of the particles is calculated according to the conventional distinct element simulation, and the normal stiffness of MH can be calculated by Equation (17).

$$k_{\mathrm{mh}} = \frac{BE_{\mathrm{m}}}{h_0} \tag{17}$$

where h_0 is the effective bond thickness that can be calculated by the equation $h_0 = (h_{\mathrm{cr}} + h_{\mathrm{cr}}^{\mathrm{max}})/2$. The MH elastic modulus E_{m} can be calculated based on Equation (18), which is strongly related to temperature T, water pressure σ_w, and MH density ρ [9].

$$E_{\mathrm{m}}/p_{\mathrm{a}} = 3(\sigma_{\mathrm{w}}/p_{\mathrm{a}}) - 1.98(T/T_0) + 4950.50(\rho/\rho_w) - 1821.78 \tag{18}$$

Therefore, the overall stiffness can be expressed by Equation (19).

$$k_{\mathrm{bn}} = \frac{k_{\mathrm{n}}BE_{\mathrm{m}}}{k_{\mathrm{n}}h_0 + 2BE_{\mathrm{m}}} \tag{19}$$

In contrast, referring to Jiang et al. [18], the tangential bond contact stiffness k_{bs} is often used in the empirical Equation (20) in the distinct element analysis:

$$k_{\mathrm{bs}} = \frac{2}{3}k_{\mathrm{bn}} \tag{20}$$

The normal stiffness is calculated by $k_{\mathrm{n}} = 4\overline{R}E_{\mathrm{c}}$, where $\overline{R}$ is the common radius of two particles, i.e. $\overline{R} = \frac{2r_1r_2}{r_1+r_2}$, and E_{c} is the nominal elastic modulus. The tangential stiffness k_{s} can be obtained based on the k_n/k_s ratio. The k_n/k_s ratio, equal to 1.5 in this study, is an empirical value. The stiffness of the bond is calculated using Eq. (17) based on our previous study [22,65,9].

Finally, according to the rolling bond model proposed by Jiang et al. [18], the rolling bond stiffness can be calculated by the following equation:

$$k_{\mathrm{bm}} = \frac{k_{\mathrm{mh}}B^2}{12} = \frac{E_{\mathrm{m}}B^3}{12h_0} \tag{21}$$

In summary, the k_{bn}, k_{bs}, and k_{bm} parameters, which are related to the effective bond thickness, can be obtained using Equations (19)–(21), respectively.

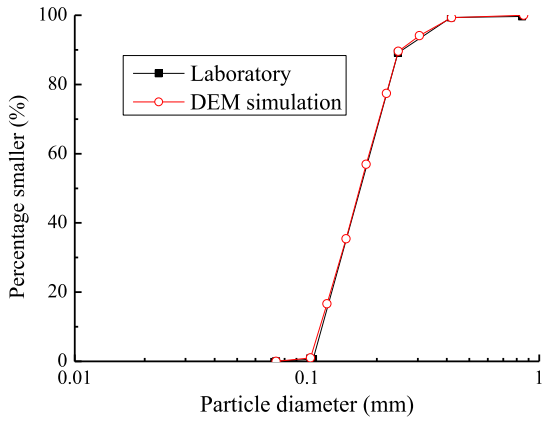

Fig. 9. Particle size distributions used in the triaxial compression tests conducted by Masui et al. [46] and DEM simulation.

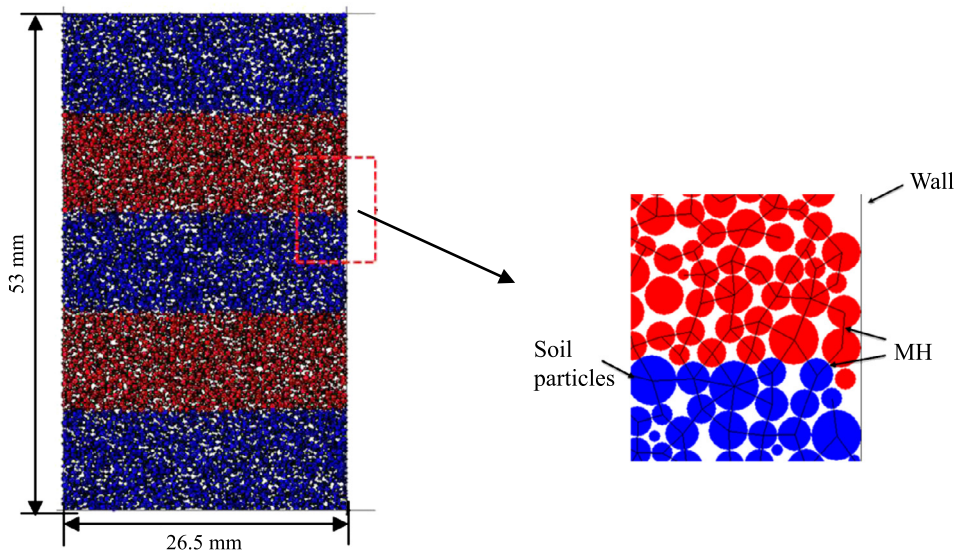

Fig. 10. DEM sample in DEM numerical simulations.

4. DEM simulation of the biaxial compression test

A series of biaxial compression tests are conducted to simulate the mechanical properties of MHBSs under different effective confining pressures (i.e. 1, 2, and 3 MPa) and MH saturations (i.e. 26%, 41%, and 55%) by incorporating the simplified THM bond model into the DEM. To compare the DEM simulation results of mechanical properties of MHBSs with those of the laboratory triaxial compression test conducted by Masui et al. [46], the conditions in the DEM simulations are taken to be the same as those in the laboratory triaxial compression test, i.e. a temperature of 5 °C and a pore pressure of 8 MPa. The particle size distribution of the Toyoura sand used by Masui et al. [46] is illustrated in Fig. 9. A close match of particle size distribution used in the DEM simulations to the laboratory grading is evident from Fig. 9.

First, the sample is generated using the multi-layer under-compaction method (UCM) proposed by Jiang et al. [73]. Fig. 10 presents the size of the DEM sample generated with a width of 26.5 mm and a height of 53 mm. Note that the color-coded grains are used to improve the visualization.

Second, when the overlap between particles is smaller than the critical bond thickness h_{cr}^{max}, the MH bonds are applied to the sample until the sample reaches the target MH saturation (i.e. $S_{MH} = 26\%$, 41%, and 55%). According to Equation (3), h_{cr}^{max} can be determined given the average particle diameter (i.e. $d_{50} = 0.1694$ mm, as illustrated in Fig. 9) and MH saturation values. As shown in Fig. 10, the variable values of h_{cr}^{max} can be obviously observed in the MHBS, represented by the black line connecting the center of two particles.

To compare the macromechanical properties of the MHBS obtained from the DEM simulation with those of the experimental results, the sand specimen parameters of the DEM simulation are firstly calibrated and obtained based on the macromechanical response of pure sand sample in the triaxial compression test. The calibration principle is that the

Table 3
Sample parameters of DEM simulation.

Diameter of particles	Fig. 9		
Sample size	26.5 mm × 53 mm	Total number in sample	20,000
Initial void ratio	0.24	Density	2.6 g/cm^3
Normal contact stiffness k_n	3.0 ×10^8 N/m	Tangential contact stiffness k_s	2.0 × 10^8 N/m
Bond width B	Equation (2)	Critical bond thickness h_{cr}^{max}	Equation (3)
Tangential bond strength R_s	Equation (9a)	Rolling bond strength R_r	Equation (9b)
Tension bond strength R_t,	Equation (15a)	Compression bond strength R_c	Equation (15b)
Bond elastic modulus E_m	2.89 × 10^8 Pa	Normal bond stiffness k_{bn}	Equation (19)
Tangential bond stiffness k_{bs}	Equation (20)	Rolling bond stiffness k_{bm}	Equation (21)
Inter-particle friction coefficient	0.5	Effective confining stress	1, 2, 3 MPa

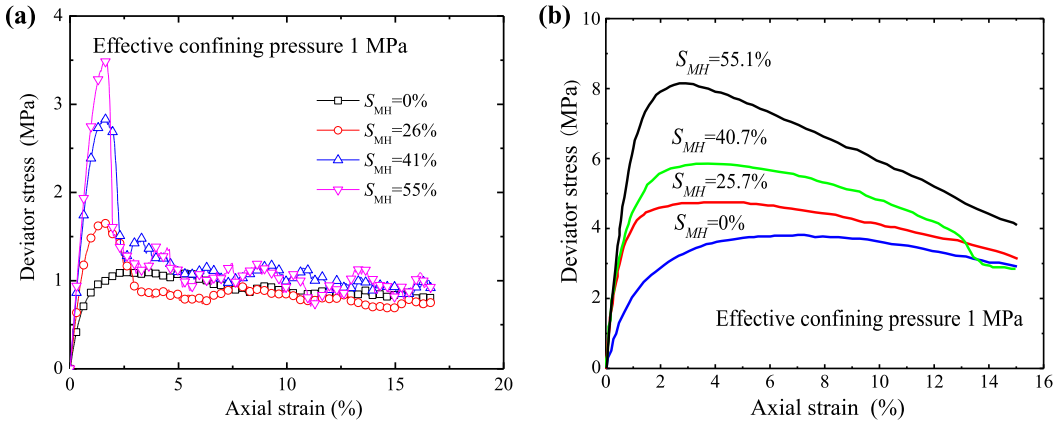

Fig. 11. Relationship between the deviator stress and the axial strain of MHBS samples under different MH saturations: (a) the DEM simulation results; (b) the results of the triaxial compression test. The graph is redrawn from Masui et al. [46].

mechanical responses (deviator stress–axial strain and volumetric strain–axial strain relations) of the DEM simulation are qualitatively consistent with that of the triaxial compression tests, as close to the actual mechanical parameters as possible.

The frictional angle is equal to $\varphi = 31°$ in the laboratory triaxial compression test. Parameters related to the specific particulate material (i.e. the interparticle coefficient of friction μ^p and particle shape factor β^p) are closely related to the mechanical strength. The calibration parameters of the particulate material are $c = 0$ MPa and $\varphi = 31°$, respectively when the corresponding parameters, i.e. the μ^p and β^p are selected to be $\mu^p = 0.5$ and $\beta^p = 2.0$, respectively. The void ratio of the granular sample is 0.24. The DEM parameters of the granular material used in this study are provided in Table 3.

The shape factor is introduced to characterize the rolling resistance strength of an unbonded contact. The physical scenario of the rolling resistance concept is as follows. Two discs are considered interacting through a finite length B, instead of a point, so that the moment can be transferred between two particles. In this way, the mechanical effects of particle shape angularity on soil behavior can be efficiently simulated with DEM. The shape factor β is used for calculating the contact length B between two adjacent particles: $B = \beta\bar{R}$, where $\bar{R}$ is the common radius of two particles, i.e. $\bar{R} = \frac{2r_1r_2}{r_1+r_2}$. See the detailed calculation of the shape factor in [74,9].

Finally, biaxial compression tests are conducted using a controlling strain loading rate of 5%/min in the quasi-static state.

5. DEM simulation results

5.1. Relationship between deviator stress and axial strain relation

Fig. 11 shows the relationship between deviator stress and axial strain under different MH saturations, with (a) presenting the results of the biaxial compression test, and (b) the triaxial compression test results obtained by Masui et al. [46]. As illustrated in Fig. 11, the macromechanical properties of MHBSs can be qualitatively captured by the simplified THM bond model considering bond thickness. With the increases of MH saturations (i.e. $S_{MH} = 26\%$, 41%, and 55%), the deviator stress increases linearly with increasing axial strain and reaches the peak deviator stress when the axial strain is about 2%. Subsequent softening behavior is observed with increasing the axial strain. With increasing MH saturation, the peak deviator stress increases and the strain softening trend is more obvious. However, the values of the residual deviator stress are similar under the different MH saturations.

The pronounced post-peak softening is a result of the quick development of localization in the simulated 2D plane deformation. This may be better understood from lab test observations where plane strain loading is often easier to implement to trigger strain localization than axisymmetric loading. As to the volumetric strain, it is the inherent flaw of 2D DEM, since the

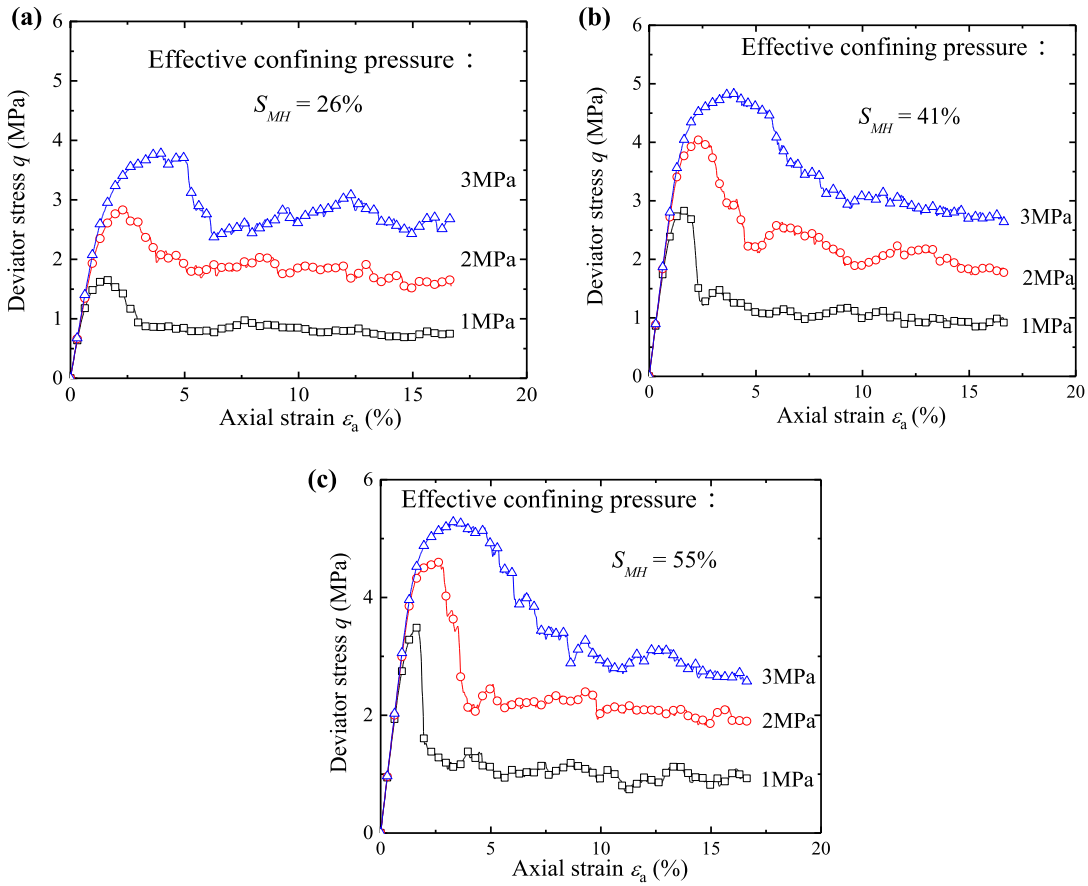

Fig. 12. Relationship between the deviator stress–axial strain of MHBS samples under different effective confining pressures and MH saturations: (a) S_{MH} = 26%; (b) S_{MH} = 41%; (c) S_{MH} = 55%.

particles cannot move spatially into adjacent voids as accurately as in 3D simulations. Due to these limitations of 2D DEM simulations, it seems meaningless to calibrate the parameters for the only purpose of matching the lab test results. Instead, the authors focused on choosing parameters based on their physical meanings. Because of the shared granular nature, the 2D DEM simulation can still capture the major mechanical features of MHBSs, particularly material failure and instability.

In addition, the mechanical properties of MHBSs are affected by the different particle-scale MH growth habits. There exist different types of MH formations such as pore-filling, cementation, or bearing loading types of MH in the laboratory MHBS specimen, while there exists only one type of formation, i.e. the cementation type of MH in our DEM simulation. Different MH formations can contribute to mitigate the destruction of MH bonds. This also results in a discrepancy between the DEM simulations and the experimental results.

Fig. 12 presents the influence of the effective confining pressure on the measured strength of the MHBS, i.e. the relationship between the deviator stress and axial strain in MH-bearing sediments for different MH saturations (i.e. S_{MH} = 26%, 41%, and 55%) at different effective confining pressures (i.e. 1 MPa, 2 MPa, and 3 MPa). The peak and residual deviator stresses increase as the effective confining pressure increases at the same value of MH saturation. Under the same effective confining pressure, the peak deviator stress increases and the subsequent softening behavior is more obvious with increasing MH saturation. A higher effective confining pressure can enhance the frictional force between the particles, thus more energy is consumed to overcome the interparticle frictional force in the triaxial compress test.

Fig. 13 shows the peak and residual strength envelopes of MH-bearing sediments with different MH saturations (i.e. S_{MH} = 26%, 41%, and 55%) under different effective confining pressures (i.e. 1 MPa, 2 MPa, and 3 MPa). At the same confining pressure, the peak shear strength obviously increases while the residual shear strength slight increases with increasing MH saturation. Fig. 14 shows the relationship between the peak friction angle φ, cohesion c, and MH saturation; the results obtained from the DEM simulation are displayed in Fig. 14(a), whereas Fig. 14(b) shows the experimental results of Masui et al. [46]. In a similar fashion to the experimental results, with increasing MH saturation, cohesion c approximately linearly increases, while the tendency of the internal friction angle is ambiguous in the DEM simulation. Methane hydrates formed between particles enhance the adhesive characteristics of host specimens, thus the cementing effect contributes to the increases in shear strength.

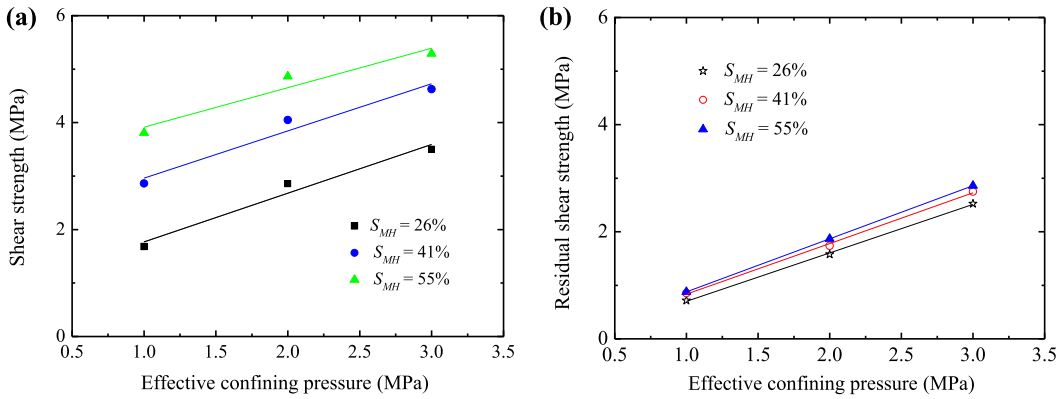

Fig. 13. Shear strength envelope of MHBS samples: (a) peak shear strength envelope; (b) residual shear strength envelope.

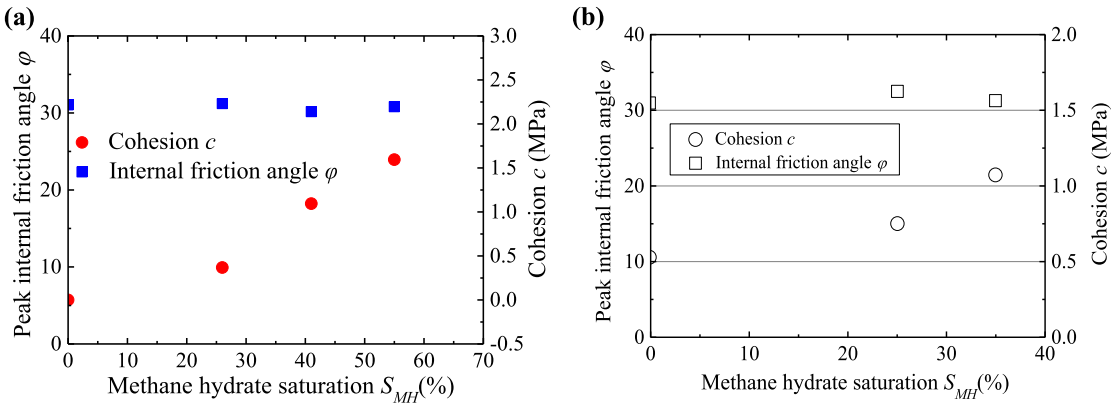

Fig. 14. Relationship between cohesion c, internal friction angle φ and MH saturation S_{MH}: (a) DEM simulation results; (b) results of the triaxial compression test conducted by Masui et al. [46].

The cementation type of MHBSs can be viewed as cemented soils based on the studies. The main behavior of MHBSs can be well captured within the scheme of cemented soils. This is why the simulated MHBS has responses similar to those of other cemented soils. Therefore, the existing constitutive model frame of cemented sand is getting the useful enlightening for proposing a proper MHBS constitutive model. However, MHBSs have some unique features other than those of cemented sand, for example: (1) the influence of particle-scale growth behavior of MH and (2) the temperature and pore (back) pressure dependency, because they directly control the strength of MH. The $h_{\mathrm{cr}}^{\max}$ studied in this paper reflects the feature of particle-scale MH growth and the extent to which MH strength controls MHBS strength (because the bond strength depends on both MH strength and bond geometry). Therefore, $h_{\mathrm{cr}}^{\max}$ is an important parameter for capturing the unique behavior of MHBSs.

5.2. Volumetric strain–axial strain relationship

Fig. 15 presents the relationship between the volumetric strain and the axial strain, in which (a), (b), and (c) are the DEM simulation results under different MH saturations (i.e. $S_{\mathrm{MH}} = 26\%$, 41%, and 55%) and effective confining pressure (i.e. 1 MPa, 2 MPa, and 3 MPa); and (d) the results of the triaxial compression test conducted by Masui et al. [46]. Fig. 15(d) shows the MHBS sample with 40.7% MH saturation demonstrates volumetric contraction and then dilatancy with the increase of axial strain. As illustrated in Fig. 15, the MHBS samples with certain MH saturation (i.e. $S_{\mathrm{MH}} = 26\%$, 41%, and 55%) show significant dilation after an initial shear contraction, in a similar fashion to the laboratory test results. With increasing MH saturation, the volumetric dilatancy becomes more obvious. The presence of MH would enhance dilation. During the compression process, MH crystals may detach form the mineral surface, and the specimen's porosity declines. The MHBS samples with MH bonds must roll across each other, which leads to the dilation of the specimens.

As to the volumetric strain, it is the inherent flaw of 2D DEM since the particles cannot move spatially into adjacent voids as accurately as in 3D simulations. However, from the viewpoint of a geotechnical researcher, 2D DEM can satisfactorily capture the strength features of soils, with carefully selected parameters, including the material failure and stability.

Fig. 16 demonstrates that the influence of the effective confining pressure on the volumetric response of MHBSs, i.e. the relationship between the volumetric strain and axial strain of MH-bearing sediments with different MH saturations (i.e.

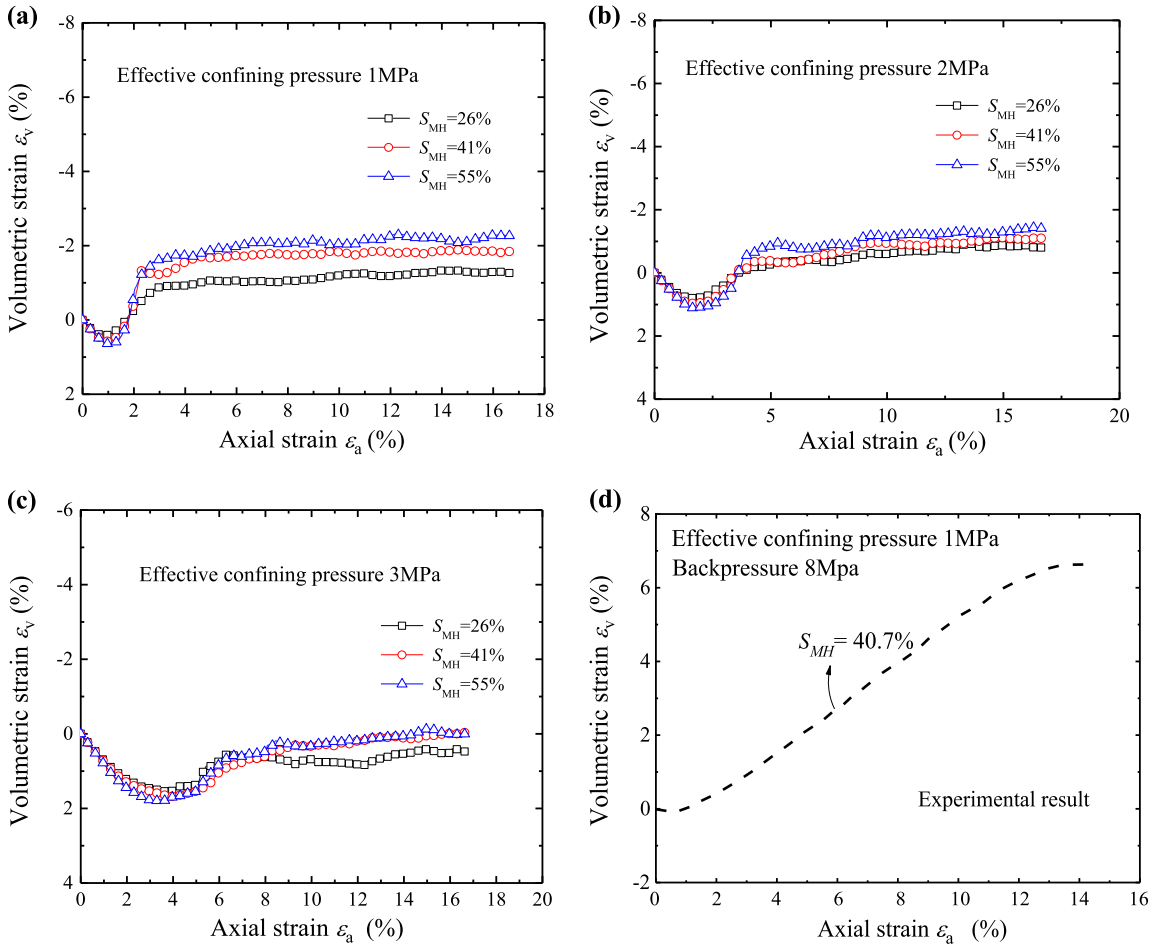

Fig. 15. Relationship between the volumetric strain and the axial strain of MHBS samples under different MH saturations: (a) 1 MPa as the effective confining pressure; (b) 2 MPa as the effective confining pressure; (c) 3 MPa as the effective confining pressure; (d) the results of the triaxial compression test conducted by Masui et al. [46].

$S_{MH} = 26\%$, 41%, and 55%) under different confining pressures (i.e. 1 MPa, 2 MPa, and 3 MPa). When the MH saturations reach 26%, 41%, and 55%, respectively, the sample firstly experiences volumetric contraction, then volumetric dilatancy. The volumetric strain shows less dilation with increasing effective confining pressure at a given axial strain. Higher effective confining pressure will increase the breakage of MH bonds and soil particles, then the particles move into the pore space during deformation, decreasing the dilation of the specimens.

5.3. Critical bond thickness

Fig. 17 demonstrates that the influence of different critical bond thicknesses (i.e. $h_{cr}^{max} = 0.00394$ mm, 0.0108 mm, 0.0137 mm, 0.0149 mm, and 0.0168 mm) on the macromechanical behaviors of MHBSs, i.e. deviator stress–volumetric strain–axial strain relation of MHBS specimen under the effective confining pressure of 1 MPa. As shown in Fig. 17(a), the strain softening characteristics of MHBSs are more obvious with the increase in the critical bond thicknesses. The critical bond thickness has a significant influence on the peak deviator stress of the MHBS. When the value of h_{cr}^{max} tends to d_{50}, i.e. h_{cr}^{max}/d_{50} approximately equals one, the peak deviator of the MHBS shows a smaller increasing tendency. These results conform to the variation tendency of MH saturations with h_{cr}^{max}/d_{50}, as illustrated in Fig. 6. The residual deviator stress of MHBSs largely remains the same at a larger axial strain under different values of h_{cr}^{max}. As illustrated in Fig. 17(b), the MHBS samples experience an apparent strain-softening behavior after an initial shear contraction. The volumetric strain shows more dilation with the increasing of critical bond thickness at a given axial strain. The variations of h_{cr}^{max} between soil particles correspond to a specific MH saturation value. It makes sense due to the peak shear strength and the dilation of the MHBS increase with increasing MH saturation.

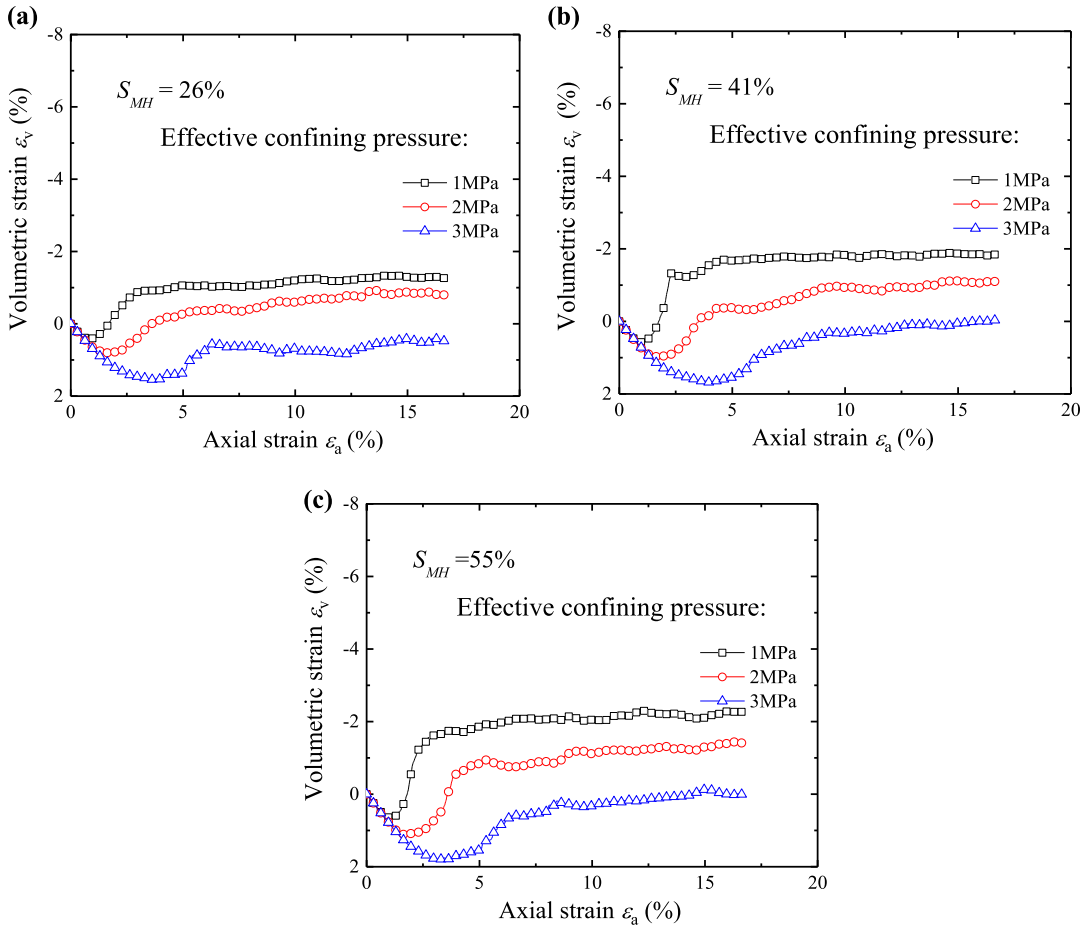

Fig. 16. Relationship between the volumetric strain and axial strain of MHBS specimens under different effective confining pressures and MH saturation: (a) S_{MH} = 26%; (b) S_{MH} = 41%; (c) S_{MH} = 55%.

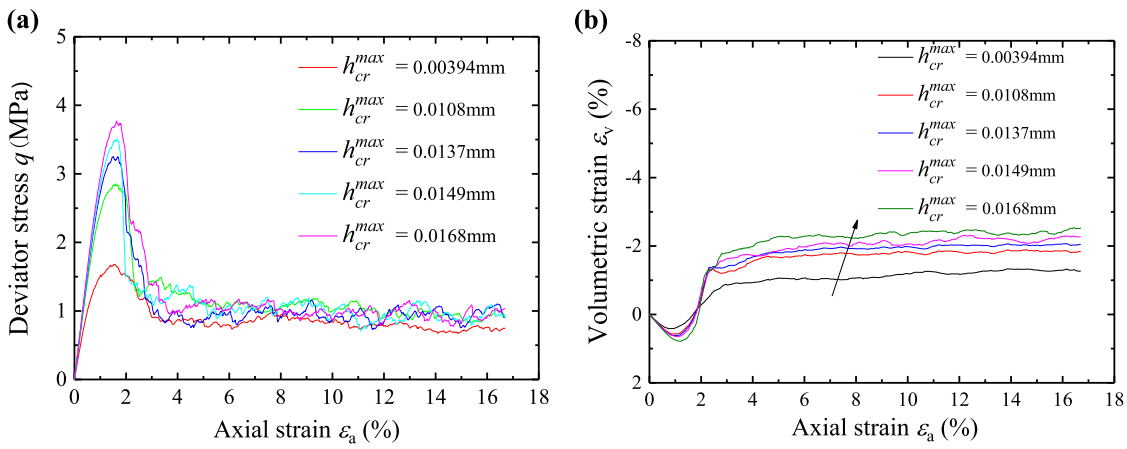

Fig. 17. Influence of different critical bond thicknesses on the mechanical behavior of the MHBS: (a) relationship between the deviator stress and the axial strain; (b) relationship between the volumetric strain and the axial strain.

5.4. Microscopic bonds

For the sake of brevity, the sample with $S_{MH} = 55\%$ under an effective confining pressure of 3 MPa is used to study the distribution of the microscopic bonds. Fig. 18(a) demonstrates the deviator stress, axial strain, and volumetric behavior of the MHBS sample with $S_{MH} = 55\%$ under an effective confining pressure of 3 MPa. Three characteristic points corresponding

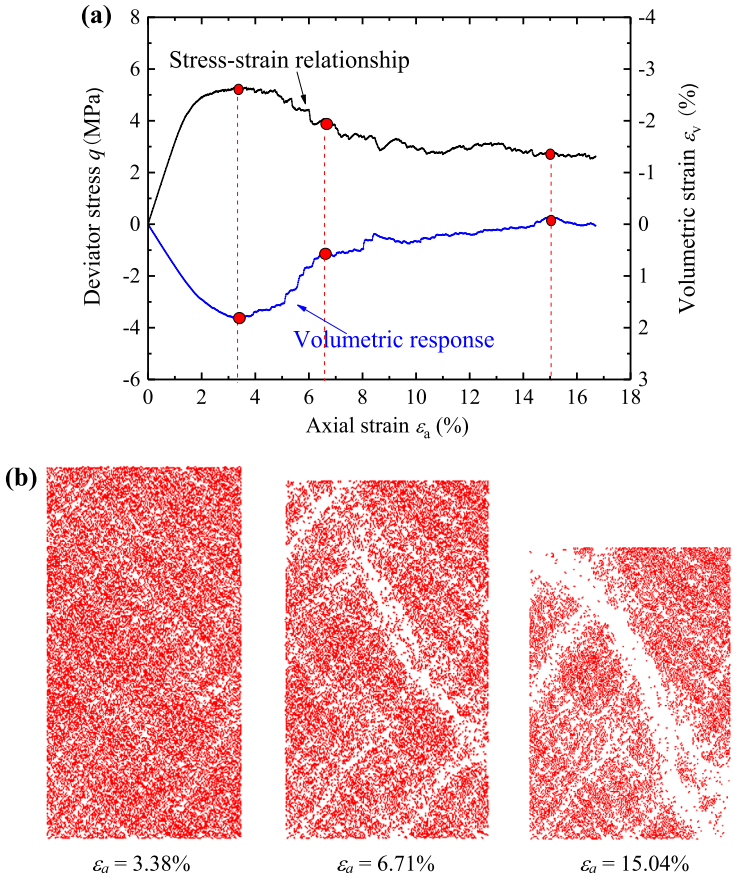

Fig. 18. (a) Deviator stress–volumetric strain–axial strain relation of an MHBS specimen with $S_{MH} = 55\%$ under the effective confining pressure of 3 MPa; (b) the distribution of the intact MH bonds at axial strains of 3.38%, 6.71%, and 15.04%.

to axial strains of 3.38%, 6.71%, and 15.04% were selected to study the macro/micromechanical responses of the MHBS, which represent the peak deviator stress and the transition from volumetric contraction to volumetric dilatancy, the deviator stress dropping from the peak to a relatively lower value, and the critical state (i.e. the deviator stress and volumetric strain remain almost constant), respectively. Fig. 18(b) presents the distribution of the intact MH bonds at different axial strains of 3.38%, 6.71%, and 15.04%. Only the intact MH bonds are marked as red solid lines at the particle contacts. A shear band develops in the sample and most of the bonds in the band break with increasing the axial strain. The percentage of broken bonds increases with the expansion of the shear band.

Fig. 19 shows the relations between the percentage of intact MH bonds, deviator stress, and the axial strain of the MHBS sample with $S_{MH} = 55\%$ under an effective confining pressure of 3 MPa. The percentage of intact MH bonds, which is defined as the ratio of the number of bonded contacts to the total number of contacts, decreases with increasing the axial strain. The deviator stress drops from the peak to a relatively lower value due to the breakage of intact MH bonds during deformation, and it gradually reaches the critical state at the axial strain of 15%.

5.5. Shear strain fields

The mesh-free methods proposed by Wang et al. [75] and Wang and Gutierrez [76] are used to measure the local strain field to account for the particle rotations and capture strain localization features with high resolution. Fig. 20 shows the distribution of the shear strain at different axial strains of 3.38%, 6.71%, and 15.04% for the 55% MH saturation sample under an effective confining pressure of 3 MPa. Clearly, a pronounced and concentrated shear band is progressively shaped in the sample, which grows thicker with increasing the axial strain. The shear behavior is distinctly restrained outside the shear band by the intact bonds. Fig. 20 implies that the evolution of the shear strain is essentially related to the bonding breakage illustrated in Fig. 18(b).

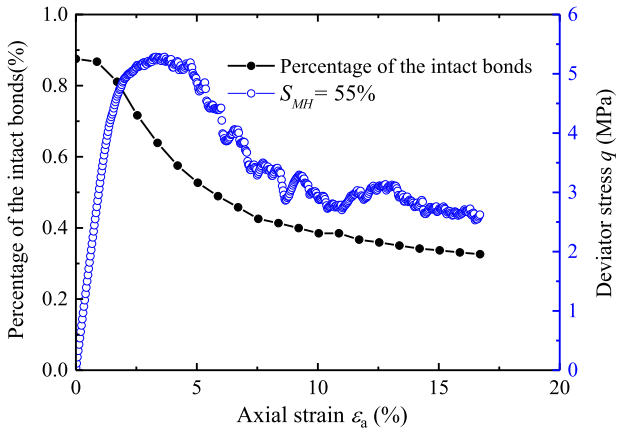

Fig. 19. Relations between percentage of the intact MH bonds, deviator stress and axial strain of an MHBS specimen with S_{MH} = 55% under the effective confining pressure of 3 MPa.

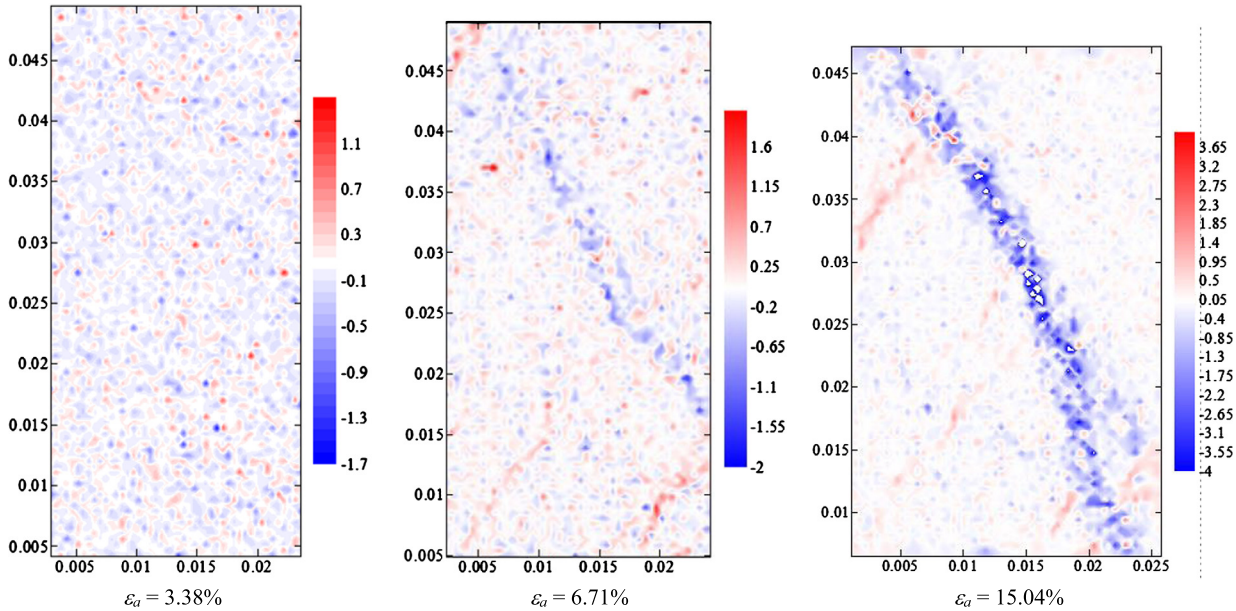

Fig. 20. Distribution of the shear strain at different axial strains of 3.38%, 6.71% and 15.04% of an MHBS specimen with S_{MH} = 55% under an effective confining pressure of 3 MPa.

5.6. Evolution of the fabric

The contact fabric ($\boldsymbol{F}_c$) is defined to characterize an assembly's microscale structure and its response during loading. $\boldsymbol{F}_c$ represents the statistical arrangement of the contact direction in an assembly. Fig. 21 presents the distribution of the contact directions at different axial strains of 0%, 2.54%, and 15.04%, with $S_{MH} = 55\%$ under the effective confining pressure of 3 MPa. With the development of axial strain, the direction of the contact between the particles forwards a vertical deflection. The deviator stress deteriorates the isotropy of the granular assemblies to induce anisotropy in terms of directional contact distribution. That is the higher proportion of contacts along the loading direction compared with contacts in the horizontal axis.

6. Conclusion

In this study, we simulated the drained biaxial compression tests to investigate the macromechanical properties of deep-sea MH-bearing soil by the DEM considering the variations of bond thickness between particles. Comparison between the numerical and experimental data shows that the macromechanical properties of deep-sea MHBSs can be reasonably and qualitatively captured by the DEM simulations. The results provide a basis for future research on the macroscopic constitutive models of MHBSs. The main conclusions are as follows.

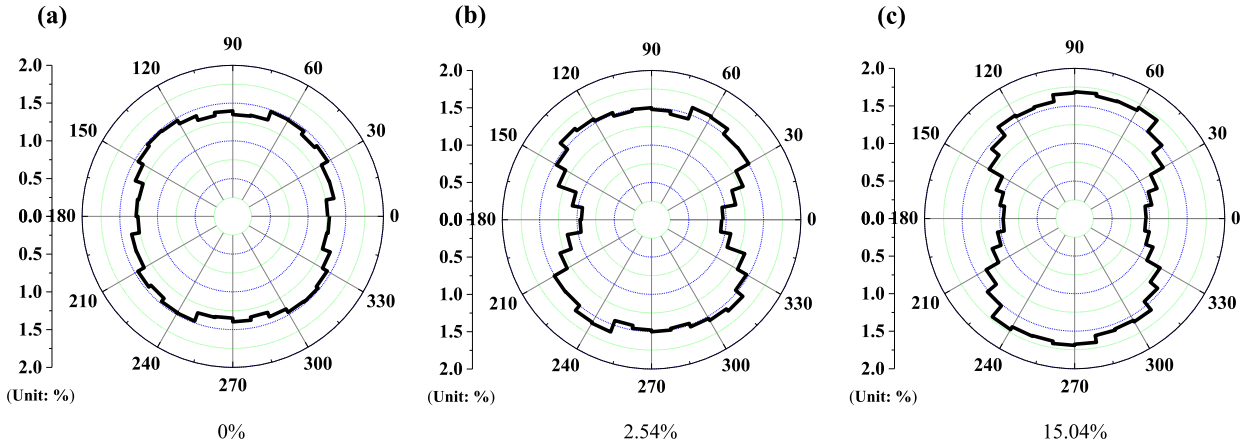

Fig. 21. Distribution of the contact directions at different axial strains of 0%, 2.54%, 15.04% with $S_{MH} = 55\%$ under an effective confining pressure of 3 MPa.

Equation (3) presents the fitting relation between the normalized hydrate critical bond thickness and the MH saturation, in which lies the bridge connecting the microscopic distributional parameter of MH to the macroscopic properties of the MHBSs.

The shear strength, cohesion, and volumetric contraction increase with increasing MH saturations, while MH saturation has little influence on the internal friction angle. The strength and volumetric contraction of MH-bearing soils increase with increasing the effective confining pressure.

The critical bond thickness has a significant influence on the peak deviator stress and dilation of the MHBS. As the critical bond thickness increases, the peak shear strength and the dilation of the MHBS increase, while the residual deviator stress of the MHBS largely remains the same at a larger axial strain.

With the increase of the axial strain, the percentage of broken bonds increases with the expansion of the shear band. The evolution of the shear strain is essentially related to bond breakage.

The deviator stress deteriorates the isotropy of the granular assemblies to induce anisotropy as the direction of the contact between the particles forwards a vertical deflection with the development of axial strain.

It should be noted that the mechanical properties of MHBSs is complex due to the different particle-scale MH growth habits. In this paper, we studied the cementation type of MHBSs based on our experiment on calcium aluminate cement. And the bond strength of these two bonding materials is different, thus the magnitude orders in terms of deviatoric stress (for example) are very different. However, the contact model in this study can well capture the main mechanical properties of MHBSs considering the variations of bond thickness between particles. Also, the mechanical properties of MHBSs are dependent on temperature and pressure, and differ from those of cemented soils [22,65,9]. In addition, it is the inherent flaw of 2D DEM, since the particles cannot move spatially into adjacent voids as accurately as in 3D simulations; the strength features of the soils can be satisfactorily captured in 2D DEM. Three-dimensional simulation to investigate the element-scale behavior of MHBSs will be our future work.

Different types of MH formations such as pore-filling, cementation, or bearing loading types of MH are existing in the natural MHBS specimens, while there exists only one type of formation, i.e. the cementation type of MH, in our DEM simulation. The macro/micromechanical behaviors of MHBSs including different types of MH need to be explored in future research.

Acknowledgements

The research was funded by the National Natural Science Foundation of China with Grant Nos. 51579178, 51379180, the National Natural Science Key Project Foundation of China with Grant No. 51639008, the Project of the State Key Laboratory for Disaster Reduction in Civil Engineering, Tongji University, of China with Grant No. SLDRCE14-A-04. All the supports are greatly appreciated. In addition, the authors thank Dr. Zhifu Shen and Ph.D. candidate Jun Liu for their valuable comments, which have improved the quality of this paper.

References

[1] Committee on Assessment of the Department of Energy's Methane Hydrate Research, and Development Program, Evaluating Methane Hydrate as a Future Energy Resource, Realizing the Energy Potential of Methane Hydrate for the United States, The National Academies Press, 2010.
[2] K.A. Kvenvolden, T.D. Lorenson, The global occurrence of natural gas hydrate, Geophysical Monograph 124 (322) (2001) 3–18.
[3] K. Soga, S.L. Lee, M.Y.A. Ng, A. Klar, Characterisation and engineering properties of methane hydrate soils, in: T.S. Tan (Ed.), Characterisation and Engineering Properties of Natural Soils, Taylor and Francis, London, 2006, pp. 2591–2642.
[4] K. Yamamoto, Methane hydrate bearing sediments: a new subject of geomechanics, in: The 12th International Conference of International Association for Computer Methods and Advances in Geomechanics, vol. 454, IACMAG, 2008, pp. 1188–1196.

[5] J.A. Priest, E.V.L. Rees, C.R.I. Clayton, Influence of gas hydrate morphology on the seismic velocities of sands, J. Geophys. Res. 114 (B11) (2009) B11205.
[6] C.R.I. Clayton, J.A. Priest, E.V.L. Rees, The effects of hydrate cement on the stiffness of some sands, Géotechnique 60 (6) (2010) 435–445.
[7] J. Brugada, Y.P. Cheng, K. Soga, J.C. Santamarina, Discrete element modelling of geomechanical behaviour of methane hydrate soils with pore-filling hydrate distribution, Granul. Matter 12 (5) (2010) 517–525.
[8] M.J. Jiang, Y.G. Sun, Q.J. Yang, A simple distinct element modeling of the mechanical behavior of methane hydrate-bearing sediments in deep seabed, Granul. Matter 15 (2) (2013) 209–220.
[9] M.J. Jiang, F.Y. Zhu, Y. Xiao, F. Liu, S. Utili, A two-dimensional bond contact model for methane hydrate bearing sediments with inter-particle cementation, Int. J. Numer. Methods Eng. 38 (17) (2014) 1823–1854.
[10] M.J. Jiang, F.Y. Zhu, S. Utili, Investigation into the effect of backpressure on the mechanical behavior of methane-hydrate-bearing sediments via DEM analyses, Comput. Geotech. 69 (2015) 551–563.
[11] M. Hyodo, J. Yoneda, N. Yoshimoto, Y. Nakata, Mechanical and dissociation properties of methane hydrate-bearing sand in deep seabed, Soil Found. 53 (2) (2013) 299–314.
[12] T. Cuccovillo, M.R. Coop, Yielding and pre-failure deformation of structured sands, Géotechnique 47 (3) (1997) 491–508.
[13] J.B. Burland, On the compressibility and shear strength of natural clays, Géotechnique 40 (3) (1990) 329–378.
[14] S. Leroueil, P.R. Vaughan, The general and congruent effects of structure in natural soils and weak rocks, Géotechnique 40 (3) (1990) 467–488.
[15] N. Estrada, A. Taboada, Yield surfaces and plastic potentials of cemented granular materials from discrete element simulations, Comput. Geotech. 49 (2013) 62–69.
[16] M.J. Jiang, D. Harris, H.H. Zhu, Future continuum models for granular materials in penetration analyses, Granul. Matter 9 (2007) 97–108.
[17] M.J. Jiang, S. Leroueil, J.M. Konrad, Yielding of microstructured geomaterial by distinct element method analysis, J. Geotech. Geoenviron. Eng. 131 (11) (2005) 1209–1213.
[18] M.J. Jiang, H.S. Yu, D. Harris, Bond rolling resistance and its effect on yielding of bonded granulates by DEM analyses, Int. J. Numer. Anal. Methods Geomech. 30 (8) (2006) 723–761.
[19] M.J. Jiang, H.S. Yu, S. Leroueil, A simple and efficient approach to capturing bonding effect in naturally microstructured sands by discrete element method, Int. J. Numer. Methods Eng. 69 (6) (2007) 1158–1193.
[20] M.J. Jiang, H.B. Yan, H.H. Zhu, S. Utili, Modeling shear behavior and strain localization in cemented sands by two-dimensional distinct element method analyses, Comput. Geotech. 38 (1) (2011) 14–29.
[21] M.J. Jiang, Y.G. Sun, Y. Xiao, An experimental investigation on the contact behavior between cemented granules, ASTM Geotech. Test. J. 35 (5) (2012) 678–690.
[22] M.J. Jiang, Y.G. Sun, L.Q. Li, H.H. Zhu, Contact behavior of idealized granules bonded in two different inter-particle distances: an experimental investigation, Mech. Mater. 55 (2012) 1–15.
[23] M.J. Jiang, F.G. Zhang, C. Thornton, A simple three-dimensional distinct element modeling of the mechanical behavior of bonded sands, Int. J. Numer. Anal. Methods Geomech. (2015).
[24] Z.J. Shen, Elasto-plastic damage model of structured clays, Chin. J. Geotechn. Eng. 15 (3) (1993) 21–28 (in Chinese).
[25] J. Kavvadas, A. Amorosi, A constitutive model for structured soils, Géotechnique 50 (3) (2000) 263–273.
[26] M. Rouainia, W.D. Muir, A kinematic hardening constitutive model for natural clays with loss of structure, Géotechnique 50 (2) (2000) 152–164.
[27] G. Rocchi, M. Fontana, M.D. Prat, Modelling of natural soft clay destruction processes using viscoplasticity theory, Géotechnique 53 (8) (2003) 729–745.
[28] B. Baudet, S. Stallebrass, A constitutive model for structured clay, Géotechnique 54 (1) (2004) 269–278.
[29] J. Suebsuk, S. Horpibulsuk, M.D. Liu, Modified Structured Cam Clay: a generalised critical state model for destructured, naturally structured and artificially structured clays, Comput. Geotech. 37 (7) (2010) 956–968.
[30] W.M. Yan, X.S. Li, A model for natural soil with bonds, Geotechnique 61 (2) (2010) 95–106.
[31] L.D. Nguyen, B. Fatahi, H. Khabbaz, A constitutive model for cemented clays capturing cementation degradation, Int. J. Plast. 56 (2014) 1–18.
[32] V. Robin, A.A. Javadi, O. Cuisinier, F. Masrouri, An effective constitutive model for lime treated soils, Comput. Geotech. 66 (2015) 189–202.
[33] F. Francisca, T.S. Yun, C. Ruppel, J.C. Santamarina, Geophysical and geotechnical properties of near-seafloor sediments in the northern Gulf of Mexico gas hydrate province, Earth Planet. Sci. Lett. 237 (3–4) (2005) 924–939.
[34] M. Hato, T. Matsuoka, H. Ikeda, T. Inamorit, T. Saeki, K. Suzuki, Geomechanical property of gas hydrate sediment in the Nankai Trough, in: Proceedings of the 6th International Conference on Gas Hydrates, 2008.
[35] S. Kataoka, S. Yamashita, T. Suzuki, T. Kawaguchi, M. Hamza, M. Shahien, Y. Ei-Mossallamy, Soils properties of the shallow type methane hydrate-bearing sediments in the Lake Baikal, in: Proceedings of the 17th International Conference on Soil Mechanics and Geotechnical Engineering, 2009, pp. 299–302.
[36] H.S. Kim, G.C. Cho, J.Y. Lee, S.J. Kim, Geotechnical and geophysical properties of deep marine fine-grained sediments recovered during the second Ulleung Basin Gas Hydrate expedition, East Sea, Korea, Mar. Pet. Geol. 47 (2013) 56–65.
[37] T.H. Kwon, K.R. Lee, G.C. Cho, J.Y. Lee, Geotechnical properties of deep oceanic sediments recovered from the hydrate occurrence regions in the Ulleung Basin, East Sea, offshore Korea, Mar. Pet. Geol. 28 (10) (2011) 1870–1883.
[38] J.A. Priest, C.R.I. Clayton, E.V.L. Rees, Potential impact of gas hydrate and its dissociation on the strength of host sediment in the Krishna–Godavari Basin, Mar. Pet. Geol. 58 (2014) 187–198.
[39] C. Puppel, R. Boswell, E. Jones, Scientific results from Gulf of Mexico Gas Hydrates Joint Industry Project Leg 1 drilling: introduction and overview, Mar. Pet. Geol. 25 (9) (2008) 819–829.
[40] J. Yoneda, A. Masui, Y. Konno, Y. Jin, K. Egawa, M. Kida, T. Ito, J. Nagao, N. Tenma, Mechanical properties of hydrate-bearing turbidite reservoir in the first gas production test site of the Eastern Nankai Trough, Mar. Pet. Geol. (2015), http://dx.doi.org/10.1016/j.marpetgeo.2015.02.029.
[41] J. Yoneda, A. Masui, Y. Konno, K. Egawa, M. Kida, T. Ito, J. Nagao, N. Tenma, Mechanical behavior of hydrate-bearing pressure–core sediments visualized under triaxial compression, Mar. Pet. Geol. (2015), http://dx.doi.org/10.1016/j.marpetgeo.2015.02.028.
[42] M. Hyodo, Y. Nakata, N. Yoshimoto, T. Ebinuma, Basic research on the mechanical behavior of methane hydrate-sediments mixture, J. Jpn. Geotech. Soc. 45 (1) (2005) 75–85.
[43] M. Hyodo, Y. Nakata, N. Yoshimoto, J. Yoneda, Mechanical behavior of methane hydrate-supported sand, in: Proceedings of the International Symposium on Geotechnical Engineering Ground Improvement and Geosynthetics for Human Security and Environmental Preservation, 2007, pp. 195–208.
[44] M. Hyodo, Y. Li, J. Yoneda, Y. Nakata, N. Yoshimoto, A. Nishimura, Effects of dissociation on the shear strength and deformation behavior of methane hydrate-bearing sediments, Mar. Pet. Geol. 51 (2014) 52–62.
[45] Y. Li, Y. Song, W. Liu, F. Yu, Experimental research on the mechanical properties of methane hydrate–ice mixtures, Energies 5 (2) (2012) 181–192.
[46] A. Masui, H. Haneda, Y. Ogata, K. Aoki, Effects of methane hydrate formation on shear strength of synthetic methane hydrate sediments, in: Proceedings of the 5th International Offshore and Polar Engineering Conference, 2005, pp. 19–24.
[47] K. Miyazaki, A. Masui, Y. Sakamoto, K. Aoki, N. Tenma, T. Yamaguchi, Triaxial compressive properties of artificial methane-hydrate-bearing sediment, J. Geophys. Res. 116 (B6) (2011) B06102.
[48] J.C. Santamarina, C. Ruppel, The impact of hydrate saturation on the mechanical, electrical, and thermal proper-ties of hydrate-bearing sand, silts, and clay, in: Proceedings of the 6th International Conference on Gas Hydrate, 2008, pp. 6–10.
[49] W.F. Waite, W.J. Winters, D.H. Mason, Methane hydrate formation in partially water-saturated Ottawa sand, Am. Mineral. 89 (8–9) (2004) 1202–1207.

[50] W.J. Winters, W.P. Dillon, I.A. Pecher, D.H. Mason, Ghastly-determining physical properties of sediment containing natural and laboratory-formed gas hydrate, in: Coastal Systems and Continental Margins, Proceedings of the Natural Gas Hydrate in Oceanic and Permafrost Environments, Kluwer Academic Publishers, 2000, pp. 311–322.
[51] X.H. Zhang, X.B. Lu, L.M. Zhang, S.Y. Wang, Q.P. Li, Experimental study on mechanical properties of methane-hydrate-bearing sediments, Acta Mech. Sin. 28 (5) (2012) 1356–1366.
[52] A.M. Tréhu, G. Bohrmann, F.R. Rack, M.E. Torres, et al., Proceedings of the Ocean Drilling Program, Initial Reports, vol. 204, College Station, Texas, 2003, Texas A & M University (Ocean Drilling Program).
[53] J.C. Santamarina, S. Dai, J. Jang, M. Terzariol, Pressure core characterization tools for hydrate-bearing sediments, Sci. Drill. 14 (4) (2012) 44–48.
[54] N.S. Nemat, N. Okada, Radiographic and microscopic observation of shear bands in granular materials, Géotechnique 51 (9) (2001) 753–765.
[55] W.W. Harris, G. Viggiani, M.A. Mooney, R.J. Finno, Use of stereo-photo-grammetry to analyze the development of shear bands in sand, ASTM Geotech. Test. J. 8 (4) (1995) 405–420.
[56] D.J. White, W.A. Take, M.D. Bolton, Soil deformation measurement using particle image velocimetry (PIV) and photogrammetry, Géotechnique 53 (7) (2003) 619–631.
[57] P.A. Cundall, O.D.L. Strack, The distinct numerical model for granular assemblies, Géotechnique 29 (1) (1979) 47–65.
[58] M.R. Kuhn, J.K. Mitchell, New perspectives on soil creep, J. Geotech. Geoenviron. Eng. 119 (3) (1993) 507–524.
[59] A. Anandarajah, On influence of fabric anisotropy on the stress–strain behaviour of clays, Comput. Geotech. 27 (1) (2000) 1–17.
[60] M.J. Jiang, H.H. Zhu, D. Harris, Classical and non-classical kinematic fields of two-dimensional penetration tests on granular ground by discrete element method analyses, Granul. Matter 10 (2008) 439–455.
[61] F. Darve, G. Servant, F. Laouafa, H.D.V. Khoa, Failure in geomaterials: continuous and discrete analyses, Comput. Methods Appl. Mech. Eng. 193 (2004) 3057–3085.
[62] M.J. Jiang, J. He, J.F. Wang, F. Liu, Distinct simulation of earth pressure against a rigid retaining wall considering inter-particle rolling resistance in sandy backfill, Granul. Matter 16 (5) (2014) 797–814.
[63] K.W. Chu, B. Wang, A.B. Yu, A. Vince, CFD–DEM modelling of multiphase flow in dense medium cyclones, Powder Technol. 193 (3) (2009) 235–247.
[64] S. Jin, S. Takeya, J. Hayashi, J. Nagao, Y. Kamata, T. Ebubyna, H. Narita, Structure analyses of artificial methane hydrate sediments by microfocus X-ray computed tomography, Jpn. J. Appl. Phys. 43 (8A) (2004) 5673–5675.
[65] M.J. Jiang, Y.P. Zhou, H. Chen, Experimental analyzes of effect of different bond thickness on parameters in micromechanical model of bonded granules, Rock Soil Mech. 34 (5) (2013) 1264–1273 (in Chinese).
[66] S. Jin, J. Nagao, S. Takeya, Y. Jin, J. Hayashi, Y. Kamata, T. Ebinuma, H. Narita, Structure investigation of methane hydrate sediments by microfocus X-ray computed tomography technique under high-pressure conditions, J. Appl. Phys. 45 (27) (2006) L714–L716.
[67] B. Shi, Easy quantitative analysis of the viscous soil microstructure, Chin. J. Hydrogeol. Eng. Geol. 1 (1997) 7–10 (in Chinese).
[68] E. Kingston, C. Clayton, J. Priest, Gas hydrate growth morphologies and their effect on the stiffness and damping of a hydrate bearing sand, in: Proceedings of the 6th International Conference on Gas Hydrates, ICGH, 2008.
[69] M.J. Jiang, J. He, J.F. Wang, B. Chareyre, F.Y. Zhu, DEM analysis of geomechanical properties of cementation type of methane hydrate bearing soils for different temperatures and pore pressures, Int. J. Geomech. 16 (3) (2016) 1–25.
[70] ASTM C845-04, Standard Specification for Expansive Hydraulic cement, Annual Book of ASTM Standards, vol. 04.01, ASTM International, West Conshohocken, PA, 2004.
[71] National Standards Association, Aluminate Cements, GB 201–2000, 2000, China.
[72] J.Y. Delenne, M.S.E. Youssoufi, F. Cherblanc, J.C. Benet, Mechanical behavior and failure of cohesive granular materials, Int. J. Numer. Anal. Methods Geomech. 28 (15) (2004) 1577–1594.
[73] M.J. Jiang, J.M. Konrad, S. Leroueil, An efficient technique for generating homogeneous specimens for DEM studies, Comput. Geotech. 30 (7) (2003) 579–597.
[74] M.J. Jiang, H.S. Yu, D. Harris, A novel discrete model for granular material incorporating rolling resistance, Comput. Geotech. 32 (5) (2005) 340–357.
[75] J. Wang, M.S. Gutierrez, J.E. Dove, Numerical studies of shear banding in interface shear tests using a new strain calculation method, Int. J. Numer. Anal. Methods Geomech. 31 (12) (2007) 1349–1366.
[76] J. Wang, M.S. Gutierrez, Discrete element simulation of direct shear specimen scale effects, Géotechnique 60 (5) (2010) 395–409.